energies

MDPI

Article

Using Machine Learning in Electrical Tomography for Building Energy Efficiency through Moisture Detection

Grzegorz Kłosowski [1,*], Anna Hoła [2], Tomasz Rymarczyk [3,4], Mariusz Mazurek [5], Konrad Niderla [3] and Magdalena Rzemieniak [1]

[1] Faculty of Management, Lublin University of Technology, 20-618 Lublin, Poland
[2] Faculty of Civil Engineering, Wrocław University of Science and Technology, 50-370 Wrocław, Poland
[3] Institute of Computer Science and Innovative Technologies, WSEI University, 20-209 Lublin, Poland
[4] Research & Development Centre Netrix S.A., 20-704 Lublin, Poland
[5] Institute of Philosophy and Sociology of the Polish Academy of Sciences, 00-330 Warsaw, Poland
* Correspondence: g.klosowski@pollub.pl

Abstract: Wet foundations and walls of buildings significantly increase the energy consumption of buildings, and the drying of walls is one of the priority activities as part of thermal modernization, along with the insulation of the facades. This article discusses the research findings of detecting moisture decomposition within building walls utilizing electrical impedance tomography (EIT) and deep learning techniques. In particular, the focus was on algorithmic models whose task is transforming voltage measurements into spatial EIT images. Two homogeneous deep learning networks were used: CNN (Convolutional Neural Network) and LSTM (Long-Short Term Memory). In addition, a new heterogeneous (hybrid) network was built with LSTM and CNN layers. Based on the reference reconstructions' simulation data, three separate neural network algorithmic models: CNN, LSTM, and the hybrid model (CNN+LSTM), were trained. Then, based on popular measures such as mean square error or correlation coefficient, the quality of the models was assessed with the reference images. The obtained research results showed that hybrid deep neural networks have great potential for solving the tomographic inverse problem. Furthermore, it has been proven that the proper joining of CNN and LSTM layers can improve the effect of EIT reconstructions.

Keywords: building energy saving; electrical tomography; moisture imaging; nondestructive evaluation; machine learning; neural networks; image processing

check for updates

Citation: Kłosowski, G.; Hoła, A.; Rymarczyk, T.; Mazurek, M.; Niderla, K.; Rzemieniak, M. Using Machine Learning in Electrical Tomography for Building Energy Efficiency through Moisture Detection. *Energies* **2023**, *16*, 1818. https://doi.org/10.3390/en16041818

Academic Editor: Umberto Berardi

Received: 28 December 2022
Revised: 22 January 2023
Accepted: 9 February 2023
Published: 11 February 2023

Copyright: © 2023 by the authors. Licensee MDPI, Basel, Switzerland. This article is an open access article distributed under the terms and conditions of the Creative Commons Attribution (CC BY) license (https://creativecommons.org/licenses/by/4.0/).

1. Introduction

The increase in energy demand and use is inextricably linked to the depletion of non-renewable resources, climate change and global warming. As a result of the climate and energy package, there is increasing pressure to reduce the negative environmental impact of electricity production, distribution and use. Consequently, the main emphasis of the European Union and Member States' strategies for improving the quality of the environment has been directed at the so-called "energy efficiency", defined as the ratio of the obtained value of the utility effect of the object, in typical operating conditions, to the amount of energy consumed by this object, necessary to achieve this effect. An increase in energy efficiency can be achieved by undertaking technical, technological, organizational and educational activities in various areas of socio-economic activity. In this research, we present an exemplary solution to increase energy efficiency in the example of the construction sector and to indicate the impact of this boost on improving the quality of life and the environment of local communities. Damp walls are one of the key factors that reduce the energy efficiency of buildings. In order to effectively remove moisture from the walls, it must have an effective method of its identification and, even better, spatial imaging of the moisture distribution. Electrical impedance tomography (EIT) supported by advanced algorithms is right for this purpose.

In this work, we compare the efficiency of convolutional neural networks (CNN), long short-term memory networks (LSTM) and mixed CNN+LSTM hybrid model. Moreover, a method for optimizing the selection of a neural network that converts electrical measurements into images from three types of neural networks is presented.

1.1. Related Works

It has been proven that electrical impedance tomography (EIT) is a proper technique for real-time saturation observation [1]. In the study [2], the authors applied the EIT technique to measure water saturation distribution within a core. They conduct experiments on a Berea sandstone core, a kind of rock used as a core sample in geologic studies, with 48 electrodes connected in three 16-electrode rings. The core was exposed to the environment, with natural imbibition causing saturation and evaporation causing desaturation. The voltage potential field was determined by passing a direct current pulse through the core and measuring the voltage potential at all electrodes, which is simply the four-wire resistance approach applied to all electrodes. The end result was a data set that showed the resistivity distribution inside the core. The resistivity distribution was then recreated using inversion, which made it possible to infer saturation.

In the publication [3], the authors compare several EIT image reconstruction algorithms. The research includes such methods as: Total Generalized Variation (TGV), Region of Interest (ROI), generalized linearization techniques, Parameter Level Set (PLS), Simulated Annealing Optimization, Genetics Algorithms, Structure-Aware Sparse Bayesian learning and D-bar with deep learning. According to the authors, among the tested methods, only two image-reconstruction algorithms are worth special attention: random theory methods and artificial neural networks, which significantly improve image quality and reflect the potential and reliability of EIT image reconstruction. The authors conclude that using machine learning and other techniques to solve nonlinear problems will improve EIT image quality by a lot in a few years as artificial intelligence improves.

Paper [4] deals with imaging moisture inside porous bricks using electrical tomography. The authors list various tomographic methods, including Electrical Resistance Tomography (ERT), which is used interchangeably with EIT. Moreover, according to the authors, the ERT (EIT) method is less expensive than other methods, less complicated and not limited to small samples. Furthermore, thanks to the small size of the equipment, it can be easily transported to various places, which makes measurements independent of the proximity of the laboratory. The effectiveness of the EIT method in imaging the moisture distribution is proven by the studies described in [5–12].

According to [13], Electrical Impedance Tomography (EIT), which was originally designed for medical applications, has recently shown promise in the development of a macro-CT technology for concrete buildings. The authors developed and verified EIT analytical methods for rectangle cement-based materials using experimental data from cubic mortar samples. As contemporary injection models, three mathematical functions (Dirac delta, Heaviside step and Gaussian) were employed. Paul Dirac discovered the Dirac delta mathematical method in 1927, the Heaviside function in the 1880s and the Gaussian function in the 1790s, so these are very old methods. Interestingly, machine learning methods were not analyzed in this current article published in 2023.

The paper [14] presents the results of comparative tests in applying the CNN and LSTM algorithms to the examination of moisture in brick walls in terms of moisture imaging. It turns out that both methods are very effective, and the differences between them are insignificant. In the article [15], the authors say that Electrical Impedance Tomography (EIT) devices are becoming more popular because they are better than other systems in a number of ways. They suggest using a resampling-based super-resolution method to improve imaging resolution. In the study [16], the authors provide a forward look at the likely important future contributions of machine learning techniques as a key translator for process knowledge to increase the capability of industrial process tomography. In [17], an electromagnetic tomography algorithm based on an autoencoder neural network of

a restricted Boltzmann machine is recommended. The purpose of this study [18] was to investigate the effects of conductivity on the performance evaluation of EIT systems. To classify the works identified in the search, a systematic review was undertaken using the Multiple Criteria Decision Analysis (MCDA). The work [19] refers to lung diagnostics using EIT. The proposed method consists of two blocks. The first block is the pre-reconstruction cases, which learn the regularization pattern from the training dataset and provide a rough reconstruction of the target. The second block is a convolutional neural network (CNN) that converts approximate targets into final images. In [20], which also refers to the EIT of lung diagnostics, Hopfield neural networks are compared to the Gauss–Newton algorithm. In [21], the authors propose a model that represents the linearized forward and inverse maps of Electrical Impedance Tomography (EIT) with a deep neural network. In their work, the authors present the use of autoencoders for denoising input measurements in EIT [22]. The utilization domain was medicine, particularly the approximation of sinograms from potential electrical data. The training of the ANN using refined inputs and coarse outputs is the subject of work [23], which makes reference to EIT. Two ANN designs based on the LeNet deep network architecture and the feed-forward fully connected ANN are suggested and compared. Paper [24] refers to using EIT to monitor load transfer across the bone cement using real-time electrical measurements. The authors show that using machine learning with EIT to describe model failure events is a good way to go. The paper [25] describes a way to build a machine-learning model based on a multilayer perceptron to solve the EIT inverse problem for imaging the crystals inside the liquid-filled reactor. The work [26] refers to EIT and presents a systematic comparison of six popular machine learning algorithms: Gradient Boosting, K-Nearest Neighbors, Random Forest, Ada Boost, Elastic Net, and Artificial Neural Network. Work [27] is another example of research using EIT in relation to solids, but the tested object is graphene, an example of a 2D material. The article [28] describes research on electrical resistivity tomography using the original CNN architecture with an additional layer and residual block to solve the inverse problem. The model presented is successfully applied to invert a field dataset acquired for levee monitoring along the Parma River in Colorno (Italy). Work [29] refers to electrical resistivity tomography. The authors demonstrate that an artificial neural network is an acceptable machine learning approach for connecting electrical conductivity to soil water content. The Rhoades model, which is a commonly used petrophysical relationship, is used to test how reliable and useful the artificial neural network technique is. In the review paper [30] on various applications of electrical impedance tomography, the authors cite examples from the field of civil engineering directly concerning the applicability of EIT for the detection of brick wall dampness in actual buildings.

1.2. Historical Building as a Research Object

Due to the increasing legal requirements regarding the reduction in energy Methodology for the in Situ Testing of the Moisture Content of Brick Walls es and the increasing environmental awareness of societies and broadly understood technological development, it is required to minimize the energy consumed in buildings. Therefore, the regulations in force in Poland, by EC Directive 89/106/EEC, define the so-called basic requirements, imposing the obligation to design and build buildings to ensure energy savings and thus—also an appropriate level of thermal insulation of partitions (Directive of the European Parliament 2002/91WE). Heat losses depend mainly on the partition's degree of insulation (considering the places of thermal bridges), ventilation efficiency, size and location of the building. Therefore, even thermal insulation designed by applicable regulations does not guarantee the elimination of excessive heat losses. Examination of the degree of moisture in brick walls is an important element of assessing the technical condition of all types of buildings, including residential and historic buildings. In these facilities, brick walls are usually very damp and salty due to the lack of anti-moisture insulation, which was not used in the past.

The moisture of the structure of the walls in architectural monuments is the most important link in their destruction, especially when the water contains aggressive, harmful admixtures. Walls with a heterogeneous structure containing hygroscopic materials become less resistant to deformation when saturated with water and lose their original strength and load-bearing capacity. Rainwater penetrates the partition through cracks, and as a result of leaks in the roofing, roofs often become damp. The lower parts of the building are also often dampened by rainwater due to water spattering from the ground. The frequency and intensity of precipitation vary over time, which makes it impossible to accurately and thoroughly predict the moisture caused by it. It has been observed, however, that it is higher in regions where precipitation and strong winds occur more often [31–33]. By soaking into the ground, they contribute to the violation of the hydrogeological system of the building's foundation. Water can also indirectly affect masonry structures [34,35]. Due to moisture's influence, steel elements' corrosion occurs [36].

As a result of capillary action, water entering parts of the building, e.g., in damp ground, can reach up to 4 m in height. When exposed to weather conditions, ceramics containing more than 1% calcium sulfate also deteriorate [37]. Studies described in the publication [35] prove that even materials containing cement with the addition of fiber-reinforced polymer lose their mechanical and strength properties due to the moisture contained in them. This confirms the general thesis of the negative impact of moisture on cement structures.

Thermal modernization and energy optimization of historic brick buildings is a basic problem, very important from a technical point of view, faced by investors, designers, and contractors during the renovation of these buildings. Therefore, before implementing appropriate protection, it is necessary to know the current moisture level of the building walls.

1.3. Overview of Methods for Identifying Moisture in Walls

In Poland, wall moisture tests are carried out using the traditional drying-weigh method and non-destructive methods. The drying-weigh method is considered the basic method, but it is destructive, requiring masonry sampling. Therefore, in Poland, many methods are also used to determine the humidity in a non-destructive way. A general breakdown of the most commonly used methods is presented in Figure 1.

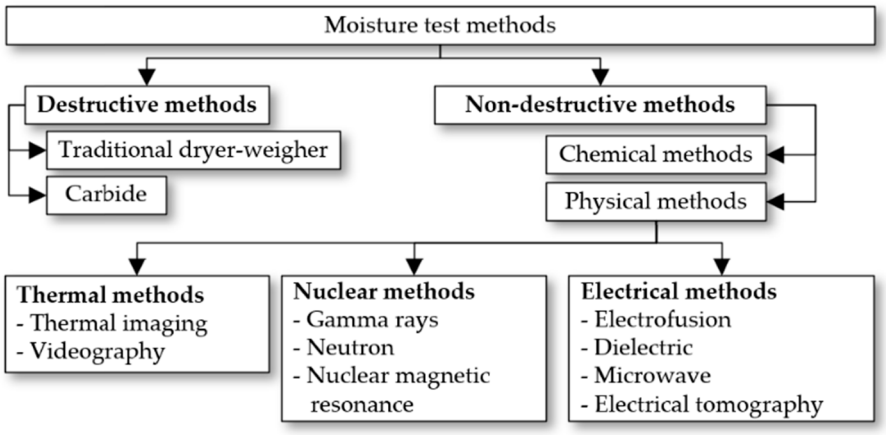


Figure 1. Division of methods for testing the humidity of materials and building partitions [36,37].

At Netrix S.A., a non-invasive method for evaluating the degree of moisture in brick walls in building structures has been developed, which enables the spatial distribution of moisture in the wall. For this purpose, we have developed a prototype of a portable hybrid tomograph (see Figure 2).

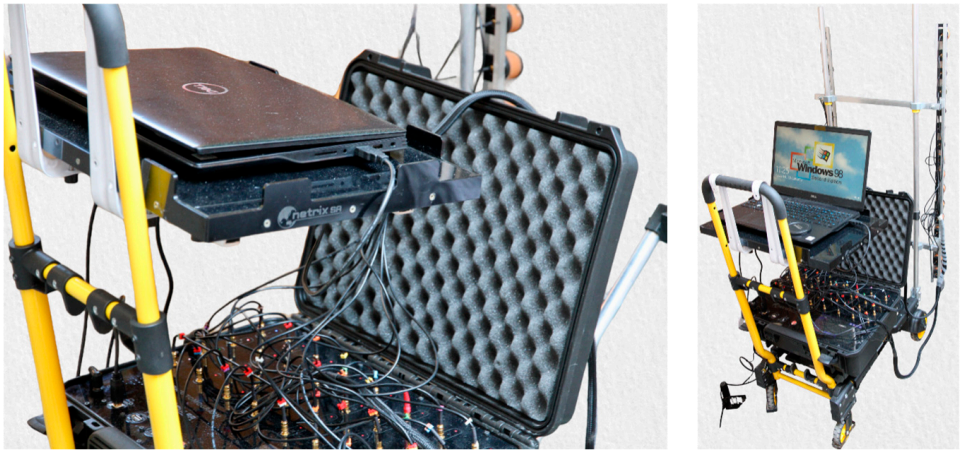


Figure 2. The mobile hybrid tomograph for testing the moisture level of building walls.

A brick wall, a spatial element with unknown parameters, is tested by a measuring system with sensors placed on the wall surfaces. Information about the distribution is obtained by repeated measurement of potentials on the object's surface with a variable location of the excitation electrodes. The method aims to obtain an image of the spatial distribution of humidity in wall elements based on measurements of the electrical properties of the material.

Tomography is the only known method for non-invasive imaging of moisture accumulated inside the wall sections [38]. The tomographic image enables the visualization of 2D wall cross-sections or 3D spatial sections [39]. None of the classic point methods makes this possible. Currently, among all tomographic methods, medical computed tomography (CT) is the most recognizable [40], but industrial/process tomography is gaining importance with information technology development. There are many types of tomography depending on the physical medium used. Within the broad group of methods included in electrical tomography, three types can be distinguished: electrical impedance tomography (EIT) [41], electrical resistivity tomography (ERT) [42–44] and electrical capacitance tomography (ECT) [45]. EIT and ERT are very similar and do not differ regarding the physical phenomena used. The voltage between the individual pairs of current electrodes is measured in both cases. Voltage changes result from different electrical resistance depending on the moisture level in the tested environment, which may be brick, masonry or soil. The difference between EIT and ERT stems from the common practice of using ERT to represent geologic differences, such as soil lithology, fracture zones, groundwater, differences in soil saturation, areas of elevated salinity or, under certain circumstances, groundwater contamination. EIT is used in industry (process tomography) and in detecting moisture inside the walls of buildings. In addition, ECT is widely used in industry and detecting dampness in bricks and walls [45–50]. ECT determines the permittivity of individual pixels or parts of a finite element mesh. The EIT and ERT methods let it see the electrical conductivity distribution in real-time [51]. In the area of problems related to detecting moisture in the walls of buildings, electrical tomography is the main application. However, there are other types of tomography whose potential has already been proven in medical and industrial applications. Additional types of tomography can be categorized based on the physical phenomenon employed. X-rays [52], ultrasonography [53], magnetism [54–56] and electromagnetic waves, including light [57,58], are examples of these.

Due to the porosity of bricks and masonry walls, EIT is the most widely utilized type of tomography to assess moisture content. Therefore, the studies discussed in this article are also EIT-related. In addition, a summary of the advantages of the EIT compared to other alternative tomographic methods in the context of detecting moisture in building walls is included in the paper [59].

In each type of tomography, the key role is played by transforming the measurement values obtained from probes placed on the surface of the tested object into reconstructive

images. This task is known as the "inverse problem," which is usually an underdetermined problem [60,61]. This problem is complicated to solve mathematically because the number and quality of input variables are insufficient to obtain an unambiguous representation in the form of a tomographic image. Such problems are solved by the finite element method, where the tested object is divided into a triangular mesh of finite elements (pixels). This study used the Eidors toolbox with Matlab R2022b software [62]. In the case of EIT, the inputs are real values correlated with the voltages measured between different pairs of electrodes, while the output values are correlated with the electrical conductivity of individual finite elements. Two strategies for solving the tomographic inverse problem are direct and indirect. The first non-iterative group includes, among others, the following examples of methods: level set [63], total variation [59] and Gauss–Newton [64]. In addition, least absolute shrinkage and selection operator, logistic regression [65], linear regression, least-angle regression [64], sparse Bayesian learning [60,66], elastic-net [59,64], support vector machines, multilayer perceptron [30] and others are popular machine learning (indirect) methods. Recently, there has been growing interest in the use of deep neural networks, including Convolutional Neural Networks (CNN) [67] and recurrent Long Short-Term Memory (LSTM) networks [51] in electrical tomography.

The research aimed to develop a deep learning model using the features of Convolutional Neural Networks (CNN) and Long Short-Term Memory (LSTM) networks, which will allow us to improve the quality of EIT reconstruction in the problem of detecting moisture inside the walls of buildings. In addition, the great advantage of EIT techniques is the possibility of automating processes through integration with industrial cyber–physical systems [68].

The novelty of the presented research is using a deep neural network algorithm containing both the CNN and LSTM layers. An original deep hybrid neural network (CNN+LSTM) was developed and then confronted with homogeneous CNN and LSTM networks. Comparing the results of the obtained reconstruction images showed that the proper combination of the CNN and LSTM layers increases the quality of the predictive model. We achieved synergy from the proper combination of two different deep-learning techniques. This research shows that combining data processing methods that seem very different can unlock new hidden possibilities in measurement data.

The comparative assessment of the hybrid network was carried out to guarantee objectivity. For this purpose, the learning parameters were kept the same while training the three CNN, LSTM and CNN+LSTM models. In addition, the same layers (CNN and LSTM) used in the homogeneous models were also used in the CNN+LSTM hybrid model.

The structure of the paper includes four sections. In the introduction are descriptions of the adverse effects of dampness in buildings, broken down into the spheres of health, economy, and construction safety. Moreover, known methods of identifying and measuring wall moisture content are presented, emphasizing tomographic methods. A short review of the algorithmic methods used in tomography was made. Section 2: Materials and Methods describes how to perform EIT measurements. This section presents the results of validation tests of wall moisture content conducted in a historic building, which was used to verify the quality of the new CNN+LSTM hybrid method. The algorithmic method of generating measurement data and the structure of the machine learning models are explained in detail. The third part of the paper refers to the results obtained with the new hybrid method compared to the two homogeneous methods. The findings presented in images and numerical indicators include reconstructions based on actual measurements of the voltages between the pairs of electrodes and images obtained from simulation measurements. Section 4 discusses the aspects of model comparability and the reasons for the advantage of the CNN+LSTM method. In addition, a classifier was suggested that makes it possible to choose the best method for a given measurement case. The fifth section summarizes the most important aspects of the research, results and conclusions. Plans for future research were also presented.

2. Materials and Methods

Technical and hardware details of the tomograph used in the present tests are described in [69], Section "2.2. Hardware description of the EIT system". The EIT system, which includes two electrode bars with 16 sensors each, a current generator, a measurement block, a multiplexer and a controller, was employed in this study. The EIT electrode system is shown in Figure 3. Sixteen electrodes placed in the metal bar were numbered sequentially and set at equal distances in a linear pattern. All combinations of connecting the power supply to subsequent pairs of electrodes are tested. During this time, other electrodes are used to measure the voltage. Figure 3a,b show two more example measurement cycles for both components, resulting in the corresponding measurement set. There are 16 choices for connecting the power supply for a system with 16 electrodes (let us denote them as the variable n), but due to the system's symmetry, we accept only half of them $(n/2) = 8$.

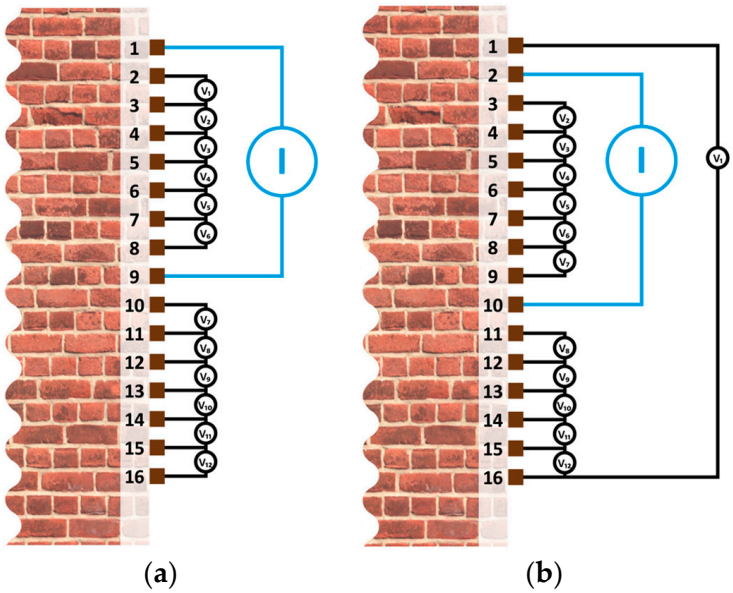


Figure 3. Performing the EIT measurement cycle with a set of 16 electrodes: (**a**) previous measurement step; (**b**) next measurement step [64].

The picture reconstruction algorithm uses voltage measurements between successive electrodes as input data. Every electric current injection into a specific pair of electrodes is called the projection angle. Due to the unknown voltage value between these electrodes, measurements performed on electrodes with an associated excitation source are ignored. A total of $n - 4 = 12$ independent measurements can be obtained for a system with $n = 16$ electrodes and any projection angle. Thus, at $n/2 = 8$ projection angles, the total number of voltages measured between successive electrodes is $(n - 4)\cdot(n/2) = 12\cdot 8 = 96$. The first and second projection angles correspond to measuring inter-electrode voltages shown in Figure 3. The power supply and measurement circuits are switched to the electrodes next to each other for each projection angle.

A device with $n = 32$ electrodes and any projection angle can produce $n - 4 = 28$ independent measurements. As a result, for $n/2 = 16$ projection angles, the total number of independent voltage measurements between adjacent voltage electrodes is $(n - 4)\cdot(n/2) = 28\cdot 16 = 448$.

The current distribution influences the electrode potentials (voltages) in the tested wall segment and the conductivity distribution. The computer image reconstruction approach recreates a conductivity distribution on a finite element mesh with predicted inter-electrode voltages near the corresponding measurement values.

The potential drop on the electrodes is relatively minimal with surface electrodes, the tested item (brick wall) has a low conductivity, and the electrodes have a high conductivity. As a result, the voltage drop is insignificant, and the electrode surface impedance coefficient

approaches zero and is negligible, but it is still considered in the reconstruction process (algorithm). Furthermore, although it has little effect on the measurement, the contact impedance is also modeled. Finally, the above steps are repeated until the current excites all nearby electrodes. As a result, 448 voltages are recorded.

The contact impedance of the electrodes with the wall has a negligible effect on voltage measurements. The reason is the voltmeters' high input impedance and the ammeters' low impedance. In addition, the output impedance of the current source is much higher than the impedance of the voltage source. Therefore, instead of applying voltages and measuring currents in most EIT systems, it injects current and measures voltages.

According to Maxwell's equations, the relationship between measurements (electric potential) with respect to conductivity is defined by the relation (1)

$$\begin{cases} \nabla \cdot (\sigma \cdot \nabla \varphi) = 0 \\ \sigma \frac{\partial \varphi}{\partial n}\Big|_{\partial\Omega} = +\mathrm{I} \\ \sigma \frac{\partial \varphi}{\partial n}\Big|_{\partial\Omega} = -\mathrm{I} \end{cases} \quad (1)$$

where n is a given boundary, "$\nabla\cdot$" is the divergence, σ is the conductivity distribution function that should be solved, φ denotes the potential in the measured field, $\nabla\varphi$ is the electrical potential gradient, and Ω signifies the whole field measured. The terms "$-$I" and "$+$I" denote the current flow from and to the electrode.

2.1. Historical Building as a Research Object

The research object was the brick walls of the medieval Cistercian abbey in Pelplin, Poland. During the in situ tests, several stations were designated and subjected to tomographic and dielectric tests to detect moisture inside the walls. Figure 4 shows the external view of the examined historical building.



Figure 4. The buildings of the Cistercian abbey in Pelplin—outer view.

Figure 5 shows a horizontal top view of the 15th-century Cistercian abbey cloisters. From among many research stands, this paper presents the results of tests performed at stand F.1b (3R, 3L) on the eastern wall of the cloisters.

Figure 6a shows the interior of the east wing of the cloisters, and Figure 6b shows the EIT system with two vertical electrode strips applied to the tested wall. The brick wall thickness in the tested place exceeds 70 cm. The image shows two vertical metal bars with electrodes 45 cm apart. Each of them contains sixteen electrodes. The design of the electrodes ensures good contact with the tested wall.

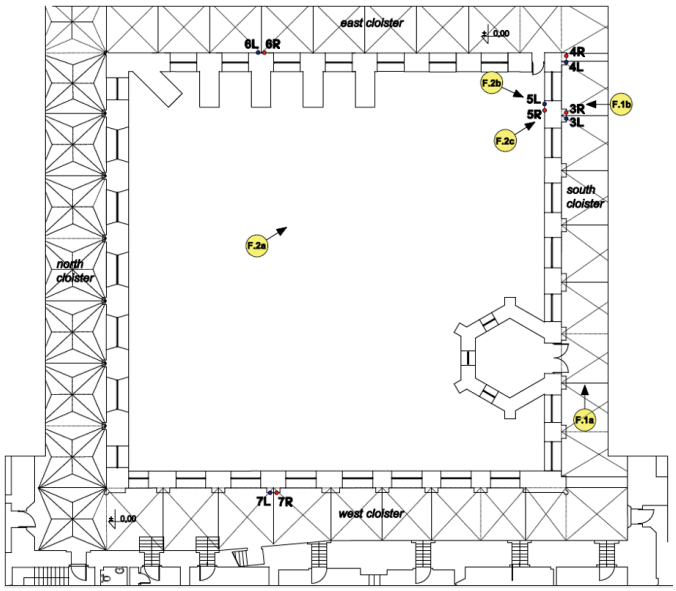


Figure 5. Floor plan of the cloisters with marked places of measurements. The presented research was carried out on stand F.1b (3R, 3L).



(**a**) (**b**)

Figure 6. The interior of the Cistercian abbey in Pelplin: (**a**) the cloisters; (**b**) EIT measurement station.

A flexible body with an adjustable handle, a flexible joint in which the connection socket is mounted, and a shock-absorbing sponge make up the electrode system. 3D printing was used to construct the plastic parts. They are held together by two sleeves, one within the other, and a flange on the upper sleeve prevents them from splitting. In addition, a rubber ring has been installed between the sleeves to ensure the body's flexibility. Such a solution allows the elements to move along an axis for each other. Polyurethane foam was used as a connector between the body and the electrode. The spongy foam material makes the entire electrode system more flexible, making it easier for the electrodes to contact the wall under test [51]. Detailed descriptions of the hardware of the EIT system used in these studies can be found in [51]. This paper focuses on logarithmic solutions.

2.2. Validation Measurements

As already mentioned, the wall humidity tests were carried out in a historic building. In order to reliably evaluate the algorithmic methods that convert the input tomographic measurements into output images, the CNN, LSTM and CNN+LSTM (hybrid model) deep learning methods were compared. When examining the humidity of an actual historical object using the new EIT system, the results of validation measurements should be available. It is essential to order to verify the effectiveness of the EIT system. Validation measurements were made using a dielectric meter that performs indirect measurements. Similar to EIT, the dielectric method is qualitative. Compared to quantitative methods, qualitative methods do not allow for an accurate percentage measurement of the water content in the wall. The dielectric measurement makes it possible to estimate the moisture content of the upper layers of the masonry points under test, combined with knowledge of the properties of the masonry under test (brick, cement, stone, etc.). In indirect methods, we measure physical quantities other than water content. Due to the correlation of these measured physical quantities with humidity, it is possible to calculate the water content in the tested point or each grid element using appropriate conversion factors. As mentioned before, the main problem with current moisture measurement methods is that the measurements are spot-on. To study the humidity of a 2D flat area or 3D spatial area, determine the humidity at multiple points on the wall and then interpolate. Tomography is the only known technique that makes it possible to visualize moisture distribution inside walls. It should be emphasized that tomography does not allow quantitative determination of the moisture content. It is a qualitative method that uses colors to distinguish between areas of varying degrees of moisture. The EIT system is designed to visually present the moisture distribution inside the wall without damaging the tested wall. The precise mapping of the shape of the damp section and the location, range and intensity of the moisture confirms the effectiveness of EIT measurements.

Figure 7 shows the location of the points of moisture measurement with a dielectric meter against the background of the EIT electrodes. The measurement points tested by the dielectric method are marked with the "·" symbol. The GANN UNI 2 m (manufacturer: Gann Mess Und Regeltechnik Gmbh) was utilized, along with the B50 ball probe. The measuring device can test humidity up to 5 cm below the wall surface.

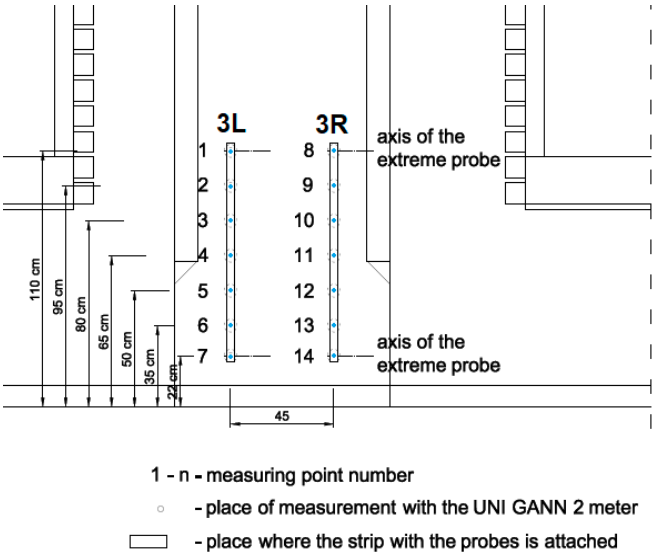


Figure 7. Validation measurement points on the tested wall section.

The dielectric meter GANN UNI 2 gives dimensionless values X_D and not the percentage of moisture U_m. These are appropriately scaled arbitrary parameters that consider the dielectric constant of the tested material (wall), which changes under the influence of moisture. Using an appropriate conversion of the dimensionless parameter X_D, it is

possible to obtain the percentage mass moisture content U_m^D. The dependence of U_m^D on the parameter X_D is determined experimentally [38].

Relation (2) presents the experimentally determined exponential function for the examined historical object.

$$U_m^D = 0.1667e^{0.0335X_D} \quad (2)$$

Table 1 contains the results of dielectric measurements that have a validation purpose. It means they were made to verify the actual measurements made by the EIT method. For example, column (1) represents the exact measurement points shown in Figure 7.

Table 1. Summary of validation measurements.

Point #	Distance from Point to the Floor	Dielectric Indication	
		X_D	U_m^D(%)
(1)	(2)	(3)	(4)
1.	22 cm above the floor level	116.6	8.19
2.	35 cm above the floor level	120.0	9.17
3.	50 cm above the floor level	119.0	8.87
4.	65 cm above the floor level	111.0	6.79
5.	80 cm above the floor level	111.7	6.95
6.	95 cm above the floor level	107.0	5.94
7.	110 cm above the floor level	102.0	5.03
8.	22 cm above the floor level	121.3	9.58
9.	35 cm above the floor level	120.0	9.17
10.	50 cm above the floor level	119.8	9.11
11.	65 cm above the floor level	112.7	7.19
12.	80 cm above the floor level	112.8	7.21
13.	95 cm above the floor level	121.4	9.61
14.	110 cm above the floor level	108.8	6.31

Column (2) shows the distances of the measurement points from the ground. Column (3) shows the dimensionless dielectric values obtained by the GANN UNI 2 m. Column (4) shows the percentages of mass moisture (U_m^D). That was found by Formula (2).

Figure 8 is a graphical presentation of the numbers included in Table 1 and shown in Figure 7. Readings from the measurement points are marked with thick circular markers. Despite some differences between the left (3L) and the right (3R), the humidity decreases as the distance from the floor increases. The dynamics of the decrease in moisture on the left side of the tested area (3L) is greater than on the right side (3R).

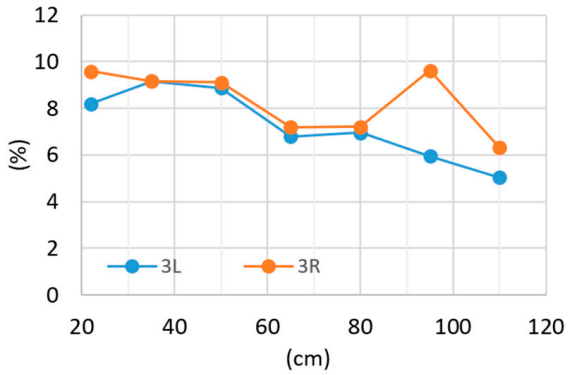


Figure 8. Point moisture according to Table 1.

An additional validation measurement was performed with a thermal camera model FLIR-T540 (FLIR Systems, Inc., Wilsonville, OR, USA). A photo of the wall of the building under study was taken with this device.

Figure 9 shows a thermal image of the wall being investigated. In the infrared photo, a damp surface is colder for evaporation. Therefore, the image clearly shows that the moisture intensity exceeds the floor level. However, it should be emphasized that the infrared images only show the state of moisture on the surface of the tested objects. Therefore, it is impossible to determine their moisture distribution based on infrared images. For this reason, infrared photos can only serve as a supplement.

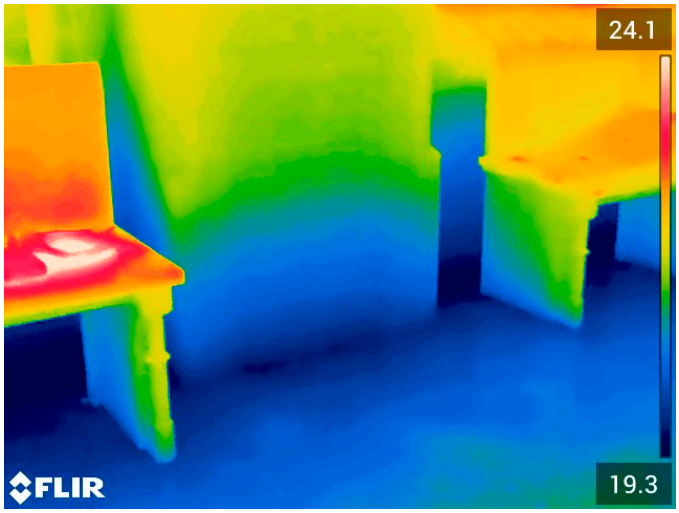


Figure 9. Thermal image of the tested wall.

2.3. Data Preparation

The predictive models were trained using a dataset generated by an algorithm. In total, 40,000 examples were developed using the simulation method to reflect the natural observations; $\frac{3}{4}$ (30,000) cases were used for training models, and $\frac{1}{4}$ (10,000) were dedicated to tests; 5% Gaussian noise was added to the measurement (input) values; 448 values represented the voltage differences between the electrode pairs in the measurement data vector. A finite element mesh divided the spatial output image into 11,297 tetrahedrons (pixels). The general concept of the model for converting measurements into EIT output images is as follows: 448 $\rightarrow$ *Model* $\rightarrow$ 11,297. The term *Model* covers three types of predictive algorithms trained in this research: CNN, LSTM and CNN+LSTM hybrid model. In this paper, a single finite element placed on a finite element mesh is synonymous with a "pixel". The simulation algorithm was created using the Finite Element Method (FEM) [60,70]. The measured voltage values were calculated based on a moisture distribution, thus solving a simple problem. The forward problem is solved by Formula (3).

$$\nabla \cdot (\sigma \cdot \nabla \varphi) = \sum_{i=1}^{3} \frac{\partial}{\partial n_i} \left(\sigma \frac{\partial \varphi}{\partial n_i} \right) = 0, \frac{\omega \varepsilon}{\sigma} "1 \quad (3)$$

Formula (3) is an extension of Formula (1). The designations of the variables are the same, with σ reflecting electrical conductivity, φ is electric potential, ω indicating angular frequency, ε means permittivity. A boundary number is satisfied by n_i, so in the case of 3D reconstruction, $n = 3$.

Figure 10 presents a synthetically generated case of moisture decomposition inside a wall section. Figure 10b shows a vector 448 input measurements with values ranging from −0.02 to +0.04. Measurement values are expressed in arbitrary units. Arbitrary units are dimensionless values that correlate with the voltages measured by the electrodes. The general purpose of tomographic testing is to illustrate the differences in moisture within the examined fragment of the wall. In other words, it is about studying the spatial changes in the distribution of a material parameter and not about determining the absolute values of this parameter. Therefore, using the direct values of the voltages measured on the

electrodes is unnecessary, which may vary significantly depending on the tested object. The EIT measurement system should detect humidity in walls with different material characteristics. Before each measurement, the electrical impedance tomography system is calibrated by adjusting the current parameters (mainly intensity, frequency and voltage) to the characteristics of the tested object (wall material, moisture level and conductivity). When using trained neural networks to convert measurements to images, there is a need to standardize the inputs to reduce the differences in their values. Therefore, we use arbitrary units instead of volts in this research.

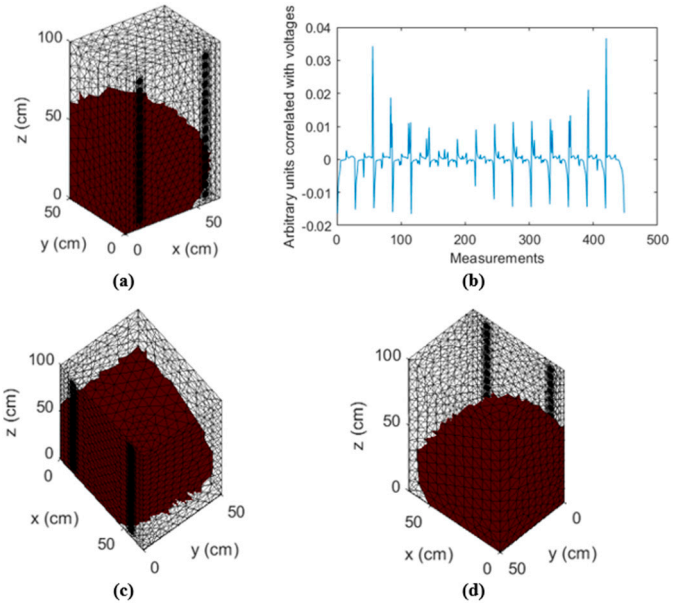


Figure 10. View of the measurement vector and the corresponding reconstructions: (**a**)—electrodes on the right, (**b**)—measurement values, (**c**)—electrodes on the left, (**d**)—electrodes on the back.

Positive and negative values of inputs result from the direction of the electric current flowing between the different electrode pairs. Random dampness (output) is created on the finite element mesh (Figure 10a,c,d). The nature of moisture is binary because dry elements have a value of 1, and wet elements have a value of 10. Pixel (finite element) values are correlated with conductivity because wet wall fragments have a lower impedance than dry ones. As shown in Figure 10b, Formula (3) allows us to solve a forward problem to figure out a vector of 448 measurements corresponding to the given moisture content.

2.4. CNN Architecture

CNN's most common applications deal with image classification. The image is saved in a 3-dimensional data array that defines each pixel's red, green and blue color components in the RGB method. An RGB image is frequently used for classification as the input layer in CNNs.

CNN used to process one-dimensional data, such as sequences or time series, is much less common. However, this does not mean that attempts to use CNN architecture to process one-dimensional data are doomed to failure. The paper is a positive example of using CNN in electrical resistance tomography [68]. Sliding convolutional filters are applied to 1D input via a 1D convolutional layer. For each fragment of the input vector, the convolution layer computes the dot product of the weights and the input values and then adds the appropriate bias. The set of weights applied to a piece of the sequence is called a filter. The filter moves along the input sequence, repeating each piece's exact computation. Thus, the filter consolidates the input data. The layer makes a convolution over the time dimension for data with three dimensions (channels, observations and time steps) that come from time series and vector sequences (data with three dimensions).

Figure 11 shows the convolution of a one-dimensional (1D) layer. Note that for the 1D input, both the filter and the output layer must also be 1D. Filter sliding is along one axis, unlike images on two axes.

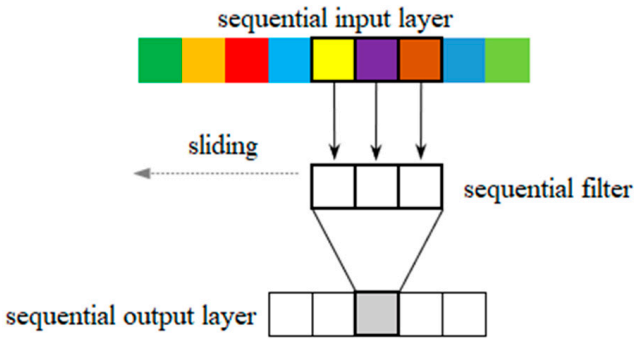


Figure 11. One-dimensional (1D) data convolution.

Table 2 presents the individual layers of the CNN network used. The first layer is a measuring vector consisting of 448 voltage values read from the electrodes of the EIT system.

Table 2. Layers of the CNN model.

#	Layers	Activations	Weights and Biases (Learnable)	Total Learnable
1	Sequence input layer with 448 dimensions	448	–	0
2	1D convolutional layer with 4 filters of size 112, stride 1, padding [4, 4]	112	Weights: 4 × 448 × 112 Bias: 1 × 112	200,816
3	Rectified Linear Unit (ReLU) layer	112	–	0
4	Dropout 30%	112	–	0
5	Batch normalization layer	112	Offset: 112 × 1 Scale: 112 × 1	224
6	1D global max pooling layer	112	–	0
7	Fully connected layer	11,297	Weights: 11,297 × 112 Bias: 11,297 × 1	1,276,561
8	Regression output layer	11,297	–	0

Since the data are compiled in one dimension (1D), they can be treated as an ordered vector, i.e., a sequence of measurement values. It is justified because the sequence of measurements from the 32 electrodes for all measurement cases is always the same. Layer (#2) is a convolution layer that converts 448 measurements into a feature map using four 112-element filters. The values of these features for a randomly selected measurement case are visualized with colors in Figure 12. "Learnable" are parameters of the model, the values determined in training the neural network. Next (#3) is the rectified linear unit layer (ReLU). Finally, ReLU defines a threshold function for each input element. Then, according to Formula (4), ReLU makes each negative value zero.

$$f(x) = \begin{cases} x, & x \geq 0 \\ 0, & x < 0 \end{cases} \quad (4)$$

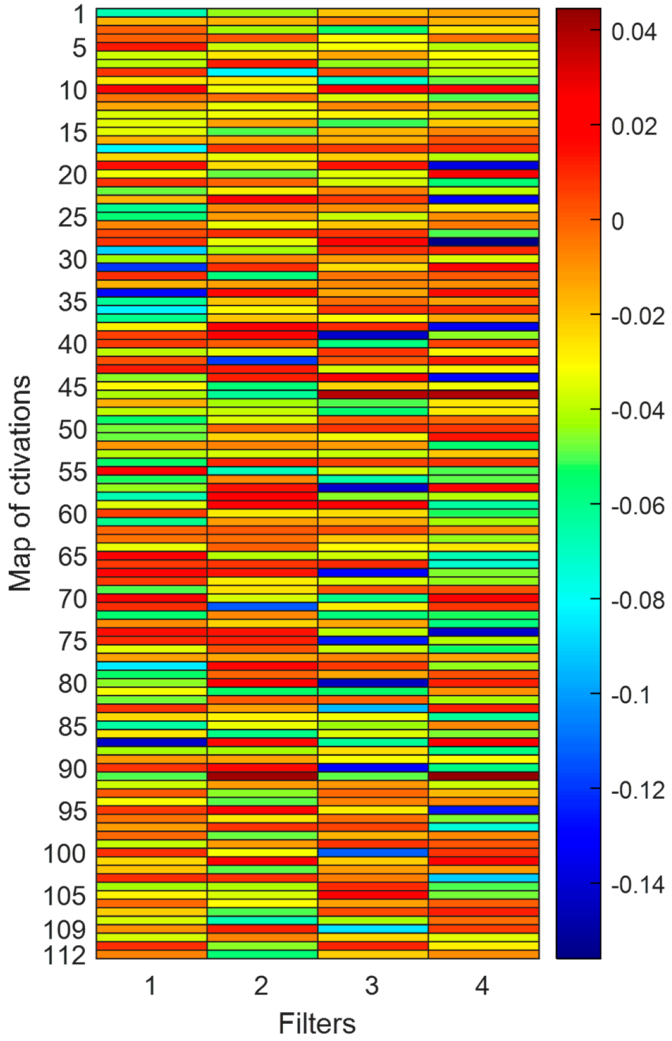


Figure 12. Activations of CNN 1D convolutional layer.

Layer (#4) is a dropout layer that randomly sets input elements to zero with a probability of 30%. This operation changes the basic network architecture to prevent overfitting of the neural network. The percentage value of the coefficient is adjusted experimentally. Too high a value leads to a reduction in the effectiveness of prediction, and too low a value may result in overfitting.

Layer (#5) is intended to normalize mini-batches of data. The normalization of the activation value is the mini-batches mean divided by the mini-batches standard deviation. Normalization is performed for each feature separately for all observations. A batch normalization layer was inserted between the model's convolution and nonlinear layers. Thanks to this placement of the normalization layer, the network learning process should be shortened. Moreover, the susceptibility of the model to network initialization should decrease. A batch normalization layer normalizes the activations and gradients propagating through the network to make neural network training better. Making more forceful parameter updates might be good as the optimization problem is simpler. If a batch normalization layer is implemented to train the model, the reconstructions in each mini-batch affect the activation of some images. Normalized activations are computed according to Formula (5)

$$\hat{x}_i = \frac{x_i - \mu_\beta}{\sqrt{\sigma_\beta^2 + \epsilon}} \tag{5}$$

where ϵ is a constant that improves numerical stability if the variance is minimal. By evaluating the mean μ_β and variance σ_β^2 for each channel/feature independently over the sequence, time and observation dimensions, the batch normalization procedure normalizes the input elements x_i. If batch normalization layers to train the model are used, the reconstructions in each mini-batch affect the activations of specific images.

After batch normalization, input data with zero mean and unit variance may not suit subsequent operations. For this reason, transformation (6) adjusts activations within the batch normalization procedure.

$$y_i = \gamma \hat{x}_i + \beta \tag{6}$$

In Formula (6), β is the shift, and γ is the scale factor. Both parameters are updated during network training, so they are learnable. Importantly, batch normalization requires a constant mean and variance to normalize the data before making predictions after training. This constant mean and variance can be determined from the training data. It can also be approximated during training with running stats calculations.

Downsampling is performed through a 1D global max-pooling layer (#6), which outputs the maximum input time or spatial dimensions. The layer pools over the time dimension for time series and vector sequence input, where data have three dimensions corresponding to the channels/features, observations and time steps. The fully connected layer (#7) multiplies the input by a weight matrix and adds the biases. The regression output layer (#8) calculates the half-mean-squared-error loss for regression tasks using Formula (7).

$$\text{Loss} = \frac{1}{2S} \sum_{i=1}^{S} \sum_{j=1}^{N} \left(y_{ij} - \hat{y}_{ij}\right)^2 \tag{7}$$

where S is the sequence length, N is the number of responses, y_{ij} is the target output for responses i,j, and $\hat{y}_{ij}$ is the reconstructed pixel. Figure 13 shows the CNN network's learning flow as the evolution of the root mean square error (RMSE). The RMSE is calculated according to Formula (8)

$$\text{RMSE} = \sqrt{\frac{\sum_{i=1}^{n} \left(y_i - \hat{y}_i\right)^2}{n}} \tag{8}$$

where n is the number of cases, y_i is the target output, and $\hat{y}_i$ is the model's prediction for response i. During 300 iterations, the RMSE value dropped to 243.7178. The numerical value of individual outputs, exemplarily assuming binary values of 1 or 10, influences the values of both indicators. Dry areas have low conductance (pixel value = 1), while moist areas have high conductance (pixel value = 10). The regular, hyperbolic shapes of the graph are undeniably a testament to the correct learning path and a prediction of no overfitting. A network trained in this manner should be able to generalize tomographic problems.

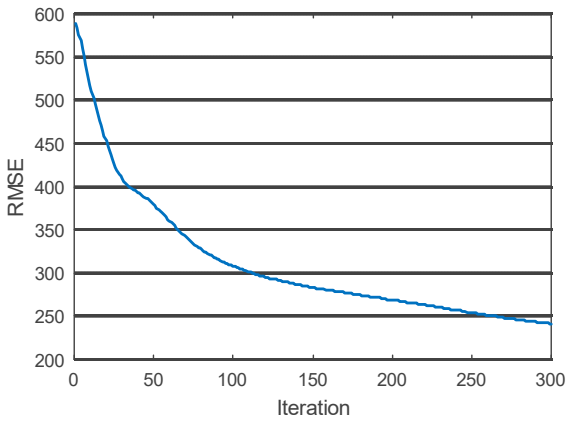


Figure 13. Training progress of the CNN.

Matlab software with the Eidors toolbox was used for the research. It was installed on a PC with an Intel Core i5-8400 CPU running at 2.80GHz, 16 GB of RAM and an NVIDIA GeForce RTX 2070 GPU. Parallel computing on the GPU was used to train the network. The total computing time of the 300 iterations with the CNN algorithm was 136 s.

Similar tests with the exact parameters of the training process (300 iterations) were also carried out for the LSTM and CNN+LSTM (hybrid) models. Ensuring that all three methods were tested the same way made it possible to compare how well they were trained.

2.5. LSTM Architecture

Figure 14 shows the LSTM layer model used in designing the EIT predictive model.

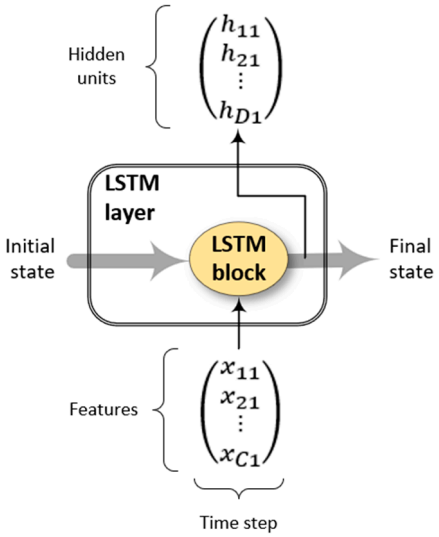


Figure 14. Structure of LSTM layer.

In the case under consideration, the entire 448-element measurement vector is treated as a single and only time step consisting of 448 features. The parameters of the LSTM layers utilized to solve the tomographic inverse problem are listed in Table 3. One bi-directional LSTM layer (Bi LSTM) with 2200 hidden units is included in the LSTM model. Experiments have demonstrated that fewer hidden units reduce network performance while adding new layers and increasing the number of hidden units lengthens the training process without improving predictive performance. The LSTM model's first layer is a one-dimensional (1D, vector) set of sequential measurement data. The Bi LSTM bi-directional layer is the following layer, which uses feedback to learn long-term correlations between sequence data in both directions. Because the network learns from the entire time series throughout each iteration, these interactions are crucial. Table 3 shows the architecture of the CNN network.

Table 3. Layers of the LSTM neural network.

#	Layers	Activations	Weights and Biases (Learnable)	Total Learnable
1	Sequence input layer with 448 dimensions	448	–	0
2	Bi LSTM layer with 2200 hidden units	4400	Input weights: 17,600 × 448 Recurrent Weights: 17,600 × 2200 Bias: 17,600 × 1	46,622,400
3	Dropout 30%	4400	–	0
4	Fully connected layer	11,297	Weights: 11,297 × 4400 Bias: 11,297 × 1	49,718,097
5	Regression output	11,297	–	0

Figure 15 shows the first 10 out of 4400 activations of the Bi LSTM layer. Again, as in Figure 12, a significant variation in the values of the activation map can be seen, which indicates a significant potential for searching for sources of valuable information within the vector of input data (measurements).

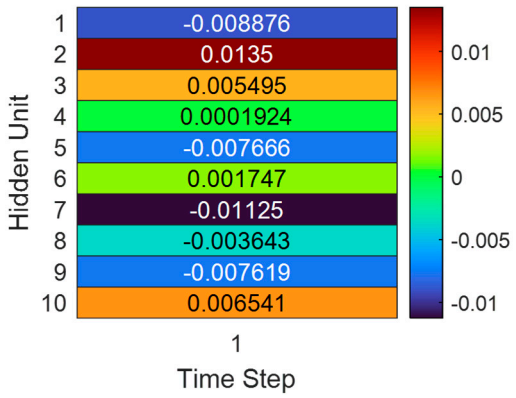


Figure 15. Activations of LSTM Layer—the first 10 out of 4400 activations.

The fourth layer is fully connected. In this layer, the weight matrix is multiplied by the numeric input values, and the bias vector is added. In the tomographic image, the fifth regression layer generates values of 11,297 pixels. Finally, color shades are created by converting the real values of pixels.

Figure 16 shows training progress during the first 300 iterations for the LSTM network and should be compared with Figure 13, which relates to CNN. The critical observation resulting from such comparison indicates a slightly worse LSTM result, for which RMSE = 280.8951.

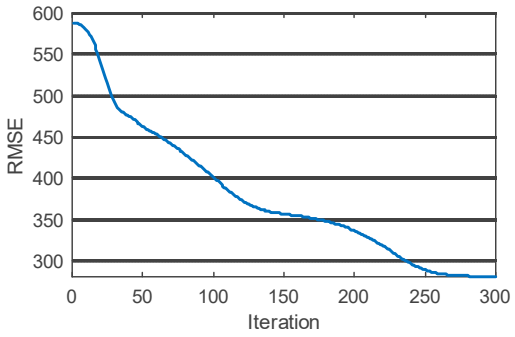


Figure 16. Training progress of the LSTM.

The total computing time of the 300 iterations with the LSTM algorithm was 348 s.

2.6. CNN+LSTM Hybrid Model Architecture

Table 4 summarizes the layers used in the hybrid model created by combining the CNN and LSTM networks. The previous sections have discussed all layer types used in the CNN+LSTM model. The first three layers in the newly created hybrid model are identical to the CNN model. Batch normalization layers have been used in rows (#3) and (#9). After the ReLU layer, the dropout and the 1D global max-pooling layers were inserted. It is also worth noting that the BiLSTM layer (#8) was placed after the 1D convolutional layer (#2). Another critical point is that the CNN+LSTM hybrid model uses two fully connected layers (#7 and #10) separated by BiLSTM and batch normalization layers.

Table 4. Layers of the CNN+LSTM hybrid neural network.

#	Layers	Activations	Weights and Biases (Learnable)	Total Learnable
1	Sequence input layer with 448 dimensions	448	–	0
2	1D convolutional layer with 4 filters of size 112, stride 1, padding [4, 4]	112	Weights: 4 × 448 × 112 Bias: 1 × 112	200,816
3	Batch normalization layer	112	Offset: 112 × 1 Scale: 112 × 1	224
4	Rectified Linear Unit (ReLU) layer	112	–	0
5	Dropout 30%	112	–	0
6	1D global max pooling layer	112	–	0
7	Fully connected layer	3000	Weights: 3000 × 112 Bias: 3000 × 1	339,000
8	Bi LSTM layer with 2200 hidden units	4400	Input weights: 17,600 × 3000 Recurrent Weights: 17,600 × 2200 Bias: 17,600 × 1	91,537,600
9	Batch normalization layer	4400	Offset: 4400 × 1 Scale: 4400 × 1	8800
10	Fully connected layer	11,297	Weights: 11,297 × 4400 Bias: 11,297 × 1	49,718,097
11	Regression output layer	11,297	–	0

Figure 17 should be compared to Figure 13 (CNN) and Figure 16 (LSTM). It turns out that the values of the indicators after 300 iterations of the learning process turned out to be the best in the case of using the hybrid model (CNN+LSTM) and were RMSE = 96.8302.

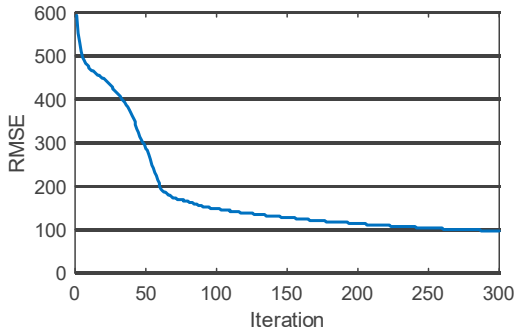


Figure 17. Training progress of the CNN+LSTM.

It is worth paying attention to the specific shape of the graph in Figure 17, which indicates a much greater learning dynamic in the initial phase of training compared to the homogeneous methods (CNN and LSTM). This feature of the hybrid model gives a clear incentive to search for the hidden potential of deep hybrid models. The total computing time of the 300 iterations with the CNN+LSTM algorithm was 570 s.

Table 5 provides a comparative overview of the training effectiveness of the three models after the first 300 iterations. The quantitative indicators RMSE and *Loss* confirm that thanks to the synergy of two homogeneous CNN and LSTM methods, the CNN+LSTM hybrid model brings the best results.

Table 5. Comparison of the training effectiveness of the three models after the first 300 iterations.

Indices \ Methods	CNN	LSTM	CNN+LSTM
RMSE	243.7178	280.8951	96.8302
Loss	2.9930×10^4	3.9408×10^4	4.6880×10^3

3. Results

Comparisons of EIT reconstructions based on actual measurements and simulated data were made to validate the CNN+LSTM hybrid approach's efficiency properly. The genuine distribution of moisture remaining inside the tested wall section is unknown. It is impossible to verify the reconstruction by comparing it with the original pattern. Only a subjective visual assessment supported by validation measurements is possible. Point measurements using traditional methods (e.g., the dielectric method) and infrared thermal photographs are the only ways to validate true tomographic readings. Spot measures are a method for estimating the consistency of tomographic image reconstruction crudely. The first section of this chapter examines reconstructions based on actual measurements taken inside a medieval building in Pelplin.

In order to objectively assess the quality of tomographic algorithms, reference images are necessary with which the reconstructive images can be compared. Thanks to the comparisons, it is possible to determine quantitative indicators that clearly show the values of errors, deviations or the level of correlation of the resulting image with the reference image. Later in this section, appropriate table summaries are provided to make it easier to analyze the found results.

3.1. Reconstructions of Real Measurements

Figure 18 shows the tomographic reconstructions obtained by measurements on the 3R/3L station, the same as in Figures 5–7 and 9. The same 448-element measurement vector was processed using the CNN, LSTM and the CNN+LSTM hybrid method. The reconstruction images (a.I), (b.I) and (c.I) show the examined fragment of the wall with dimensions of 60 × 50 × 100 cm (width, depth and height). The line containing 2D images (a.II), (b.II) and (c.II) shows the front of the examined wall section, which is not visible in the 3D images as a wall marked with the symbol "x (cm)". Figure 18(a.I–c.I,a.II–c.II) show vertical rows (2 × 16) of black dots. The dots mark the contact points of the electrodes with the surface of the tested wall. The EIT images use colors to reproduce the electrical conductivity of individual finite elements. Conductivity increases with increasing moisture. According to the colored stripes, the wet areas are dark blue and the dry areas are intensely red. The colors have been calibrated so that the color is white, around zero on the color scale. The background color is also the same (white), with blue contrasting the dampness. A clear correlation can be seen when comparing the EIT reconstructions from Figures 8 and 9. By analyzing Figure 8 as a validation pattern, it can be seen that lines 3L and 3R do not run identically. It means that moisture distribution inside the left and right sides of the tested wall section is not the same. It can be seen that the 3R line corresponding to the right side of the section indicates a greater level of moisture than the left side. The above conclusion is confirmed by all the tomographic reconstructions presented in Figure 18. The differences between the CNN, LSTM and CNN+LSTM methods concern the shape and the area covered by the dampness. However, all the images show increased humidity on the right side of the examined wall. In the case of 3D (spatial) reconstruction, it is necessary to look at the output image from many angles. It is because it is not impossible to see the areas hidden behind the foreground opaque layers of the image.

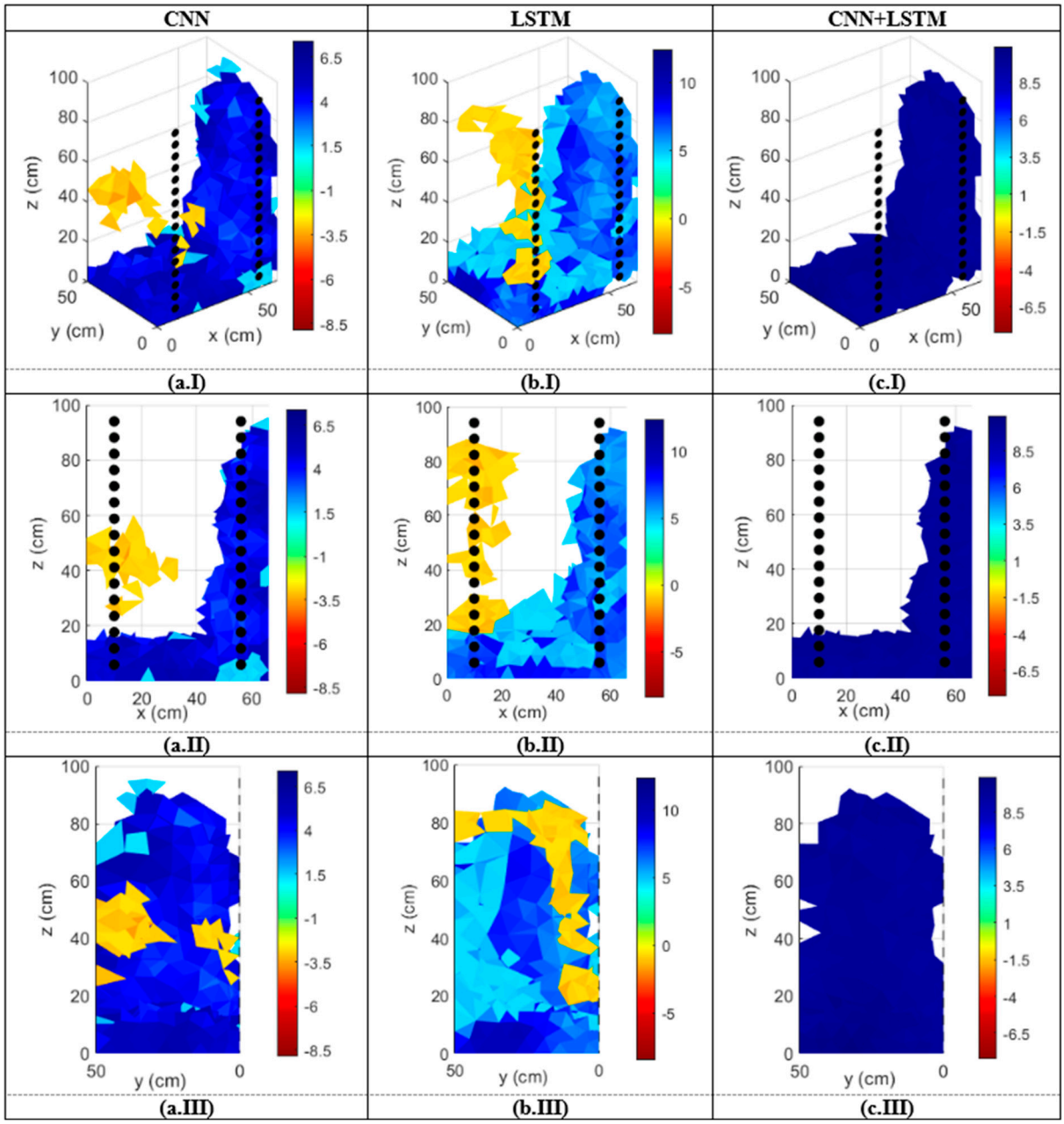


Figure 18. Reconstructions gained from real measurements: (**a.I**–**a.III**) refer to CNN, (**b.I**–**b.III**) refer to LSTM, and (**c.I**–**c.III**) refer to CNN+LSTM.

The best way to determine which of the three methods best shows how much moisture is in the wall is to pick the method based on the quantitative indicators; it has been performed in the next section describing the results of the EIT based on simulation measurements.

3.2. Reconstructions of Simulation Measurements

The ability to use accurate quantitative measures is the main advantage of testing EIT synthetic measurements' effectiveness over testing data from actual measurements. By generating measurements using the simulation algorithm, reference images are simultaneously generated. In addition, it enables the use of popular indicators such as Mean Square Error (MSE) calculated according to Formula (9), Relative Image Error (RIE) satisfied by Equation

(10), Mean Absolute Percentage Error (MAPE) given by relation (11) and Image Correlation Coefficient (ICC) expressed by Formula (12).

$$\mathrm{MSE} = \frac{\sum_{i=1}^{n}(y_i - \hat{y}_i)^2}{n} \tag{9}$$

$$\mathrm{RIE} = \frac{\|\sum_{i=1}^{n}(\hat{y}_i - y_i)\|}{\|\sum_{i=1}^{n} y_i\|} \tag{10}$$

$$\mathrm{MAPE} = \frac{1}{n}\sum_{i=1}^{n}\left|\frac{y_i - \hat{y}_i}{y_i}\right| \tag{11}$$

$$\mathrm{ICC} = \frac{\sum_{i=1}^{n}(y_i - \overline{y})(\hat{y}_i - \overline{\hat{y}})}{\sqrt{\sum_{i=1}^{n}(y_i - \overline{y})^2 \sum_{i=1}^{n}(\hat{y}_i - \overline{\hat{y}})^2}}. \tag{12}$$

In the above formulas, n means the number of finite elements, y_i is the reference of the i-th pixel, $\hat{y}_i$ is the value of the reconstructed pixel, $\overline{y}$ is the mean pattern distribution and $\overline{\hat{y}}$ is the average distribution of the reconstructed finite elements (pixels). All the above indicators were used to evaluate the four selected test reconstructions.

Table 6 shows the values of the MSE, RIE, MAPE and ICC ratios broken down into four test cases and three methods (CNN, LSTM and CNN+LSTM). The first three indicators (MSE, RIE and ICC) determine the size of deviations (errors) from the values represented by the reference images. Therefore, the smaller the above indicators are, the better the reconstructions are. The situation is different in the case of the ICC correlation index, the optimal value of 1, and the worst value is zero. The same four test cases, as presented in Table 6, are shown in Figure 19 as reconstructive images. The analysis of the indicators in Table 6 shows a clear advantage of the CNN+LSTM hybrid method over the homogeneous methods. According to all indicators, the best results were obtained using the CNN+LSTM hybrid method in all the presented cases. The average values in the bottom rows of Table 6 are fundamental. They also clearly indicate the dominance of the hybrid method.

Table 6. Indicators characterizing the quality of reconstructions for individual methods and variants.

Case	Indicator	The Method		
		CNN	**LSTM**	**CNN+LSTM**
I	MSE	6.869	4.263	0.334
	RIE	0.839	0.661	0.185
	MAPE	1.402	0.752	0.161
	ICC	0.777	0.609	0.974
II	MSE	3.837	2.386	0.200
	RIE	1.012	0.798	0.231
	MAPE	1.364	0.705	0.255
	ICC	0.384	0.413	0.953
III	MSE	4.965	2.846	0.183
	RIE	0.794	0.601	0.152
	MAPE	1.217	0.723	0.239
	ICC	0.690	0.676	0.982
IV	MSE	10.24	7.839	0.768
	RIE	0.453	0.396	0.124
	MAPE	1.173	1.213	0.333
	ICC	0.812	0.800	0.983
Average	MSE	6.477	4.333	0.371
	RIE	0.774	0.614	0.173
	MAPE	1.289	0.848	0.247
	ICC	0.665	0.624	0.973

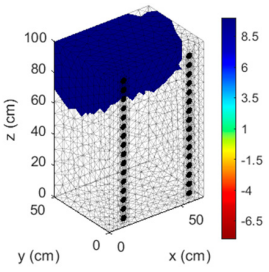
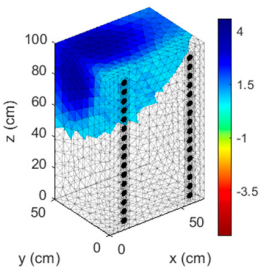
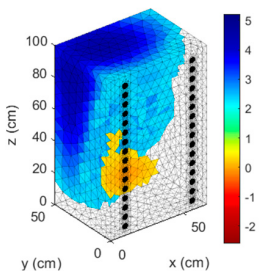
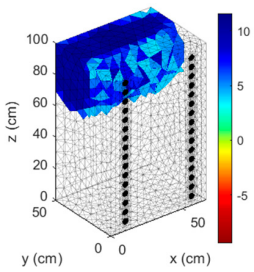
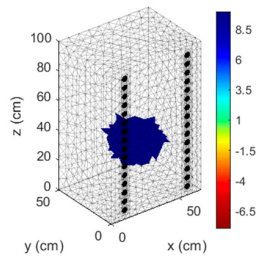
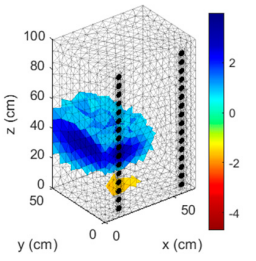
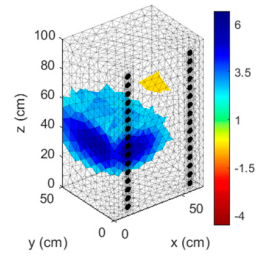
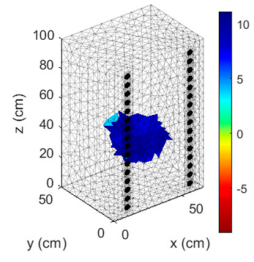
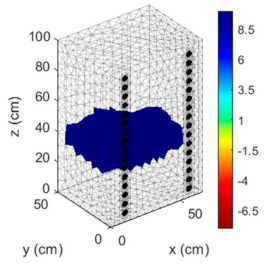
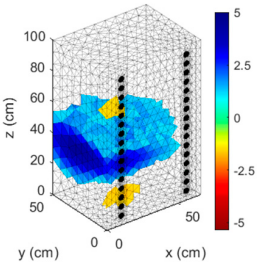
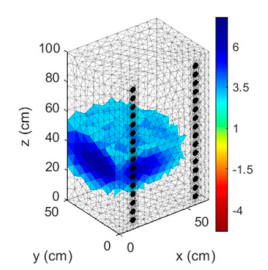
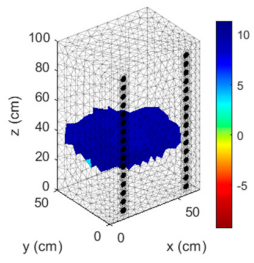
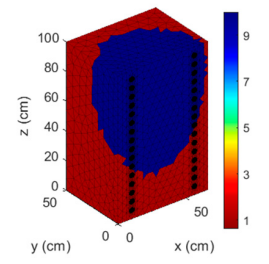
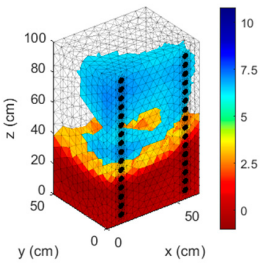
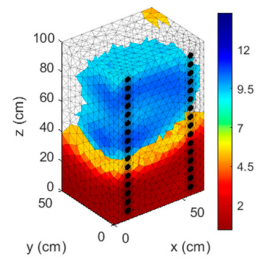
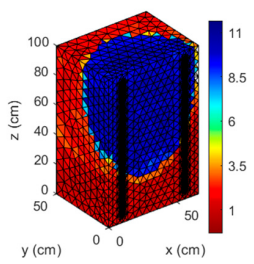
Case	Pattern	CNN	LSTM	CNN+LSTM
I				
	(**a.I**)	(**b.I**)	(**c.I**)	(**d.I**)
II				
	(**a.II**)	(**b.II**)	(**c.II**)	(**d.II**)
III				
	(**a.III**)	(**b.III**)	(**c.III**)	(**d.III**)
IV				
	(**a.IV**)	(**b.IV**)	(**c.IV**)	(**d.IV**)

Figure 19. Reconstructions of 4 cases obtained from simulation-generated measurements: (**a.I**–**a.IV**)—pattern images, (**b.I**–**b.IV**)—reconstructions using CNN, (**c.I**–**c.IV**)—reconstructions using LSTM, (**d.I**–**d.IV**)—reconstructions using a hybrid network CNN+LSTM.

The analysis of all four cases presented in Figure 19 shows that the CNN+LSTM method is the only one for which the reconstructions show no artifacts and most accurately reflect the shape and dimensions of the standard moisture. The LSTM reconstruction generated a yellow artifact in case I, while the blue shape defining the moisture frame is much larger than the reference image. The image from the CNN model is better suited than the LSTM but worse than the CNN+LSTM. Case II shows a good fit for the CNN+LSTM hybrid model and a worse fit for the CNN and LSTM models. The CNN and LSTM models show more extensive moisture than in the reference image in case III. The fit of the CNN+LSTM reconstruction is very good. In the case of IV, the model reconstruction shows very high contrast between the moist (blue) and dry (red) areas. The CNN and LSTM reconstructions are highly error-prone to the point where they do not resemble the pattern.

The CNN+LSTM reconstruction reflects the reference picture very well. In this case, the fact that the hybrid method is better than the other methods shows itself in a certain way.

It should be aware of generating colors based on the numerical values of pixels reconstructed by algorithmic methods. The tomography aims best to visualize the moisture distribution inside the tested wall. At the same time, the goal is not to measure the percentage of moisture accurately. In this case, the color palette should be matched to the numerical pixel values of the image in such a way as to reflect the differences in humidity as accurately and clearly as possible. It means, for example, that the boundaries between wet and dry areas should be visible. The division of the wall sections into wet and dry areas is also arbitrary (relative). For different test objects, different numerical values of pixels making up a tomographic image will be considered wet or dry. Therefore, color calibration in electrical tomography plays an important role.

In order to make an objective and generalized assessment of the quality of all three analyzed prediction models, the values of the MSE, RIE, MAPE and ICC coefficients were averaged for 10,000 test cases. The results are presented in Table 7. As can be seen, for all four indicators, the CNN+LSTM method gives the best results. Table 8 shows the winning method percentage according to individual criteria defined by four factors (MSE, RIE, MAPE and ICC); 10,000 test cases were investigated.

Table 7. Indicators characterizing the mean quality of testing reconstructions.

Mean Indicator	The Method		
	CNN	**LSTM**	**CNN+LSTM**
MSE	7.534	6.971	0.609
RIE	0.634	0.643	0.183
MAPE	1.306	1.453	0.299
ICC	0.753	0.602	0.913

Table 8. Percentage of the winning methods according to the indicator criteria.

Indicator	The Method (%)		
	CNN	**LSTM**	**CNN+LSTM**
MSE	0	0	100
RIE	0	0	100
MAPE	0	0	100
ICC	1.4	0.8	97.8

For the MSE, RIE and MAPE mean metrics, the hybrid CNN+LSTM method proved 100% effective in all analyzed cases. According to the mean ICC coefficient, the CNN+LSTM method did not achieve full effectiveness, but with 97.8%, it outperformed both homogeneous methods. Similarly, the CNN model scored 1.4%, and the LSTM scored 0.8%, winning among the tested cases.

Table 9 shows the training and reconstruction times of neural networks. The most significant differences are in the training times, which are of no great significance to the potential applications.

Table 9. Time of training and reconstruction of neural network models.

Models	Training Time (min)	Mean Reconstruction Time (s)
CNN	127	0.016622
LSTM	319	0.046441
CNN+LSTM	927	0.016133

The reconstruction times are similar and very short, which is advantageous because it allows measurements to be made even in dynamic environments. The mean reconstruction time was calculated based on ten random test cases. Appropriate solutions were applied to both the neural network architecture and the learning process to avoid over-learning the network. The dropout layer plays a protective role in the model structure. Securing against overfitting was the early stopping method, which automatically stops the learning process when the Loss index (7) does not drop for the assumed number of consecutive iterations. In this case, the early stopping method assumed that the trigger was eight iterations in a row.

4. Discussion

4.1. Comparability of Models

The presented studies showed a clear advantage of the CNN+LSTM hybrid method over the homogeneous CNN and LSTM methods. The outperforming of the hybrid method is strongly justified because the research took care of the comparability of all three models. First of all, identical training and testing sets were used during the training and evaluation of the models. Furthermore, when developing the model architectures, care was taken to make them comparable. In particular, the hybrid model includes one 1D convolutional layer with four filters of size 112 (stride 1, padding [4, 4]) and one Bi LSTM layer with 2200 hidden units. Both layers have the same hyperparameters as inhomogeneous networks (CNN and LSTM). In addition, all three models contain a dropout layer with a parameter of 30%. The hybrid network was deliberately not enriched with additional layers, so comparing it with homogeneous models could raise reasonable doubts.

The parameters of the training process were also the same. Adam stochastic optimization [70] with a constant learning rate of 0.001 was used to update the hyperparameters of the neural network in a loop.

4.2. Purpose and Consequence of Combining CNN and LSTM

Science has made significant progress in the development of CNN in the last several years. The dynamic development and great popularity of the LSTM network began much later than CNN, around 2016. Due to their architecture, convolutional networks are especially predisposed to solving classification problems, especially those involving recognizing images composed of pixel matrices. Modifying the last layers localized after the fully connected layer can easily change the nature of the neural network from classification to regression. It is also possible to reduce the dimensions of the CNN inputs from a multidimensional matrix to a one-dimensional (1D) vector. A convolutional neural network can process sequence data, signals, audio or time series. The essence of CNN's effectiveness lies in the triad of successive layers: convolutional, rectified linear unit (ReLU) and pooling. Thanks to specially designed square filters, features are automatically extracted. A feature map is created so this network does not require manual feature extraction as part of preprocessing. It is an advantage that, for example, LSTM networks do not have.

LSTM (long short-term memory) models have other capabilities that CNN lacks. For example, LSTM networks can learn dependencies between time steps of sequence data due to their recursiveness. For this reason, LSTM models are very good at solving problems that require signal classification or recognition of sounds.

Electrical impedance tomography measurements are sequential. In the described research, each measurement case consists of 448 values of arbitrary units correlated with voltages. It is an ordered vector because each sequence of measurements is performed in the same order and with the same frequency determined by the multiplexer. Although the test object, a fragment of a damp wall, is static, the measurement has a dynamic element because it is a sequence of measurements carried out in a specific order and at a specific time. It explains the desirability of potentially using LSTM networks in EIT imaging.

As mentioned before, the EIT measurement sequence consists of 448 values. Figure 20 shows the exemplary measurement vectors for three random reconstructions. It can seem that while the plots are different, there are periodic changes within each sequence. This phe-

nomenon indicates the existence of interdependencies between the individual measurement values within a single sequence. Therefore, if there are dependencies between the values of consecutive measurements, this is the reason to use the LSTM network. The measurement sequence plots also have visual symmetry features regarding the x-axis and the y-axis. This visual ordering gives the potential for CNN, which extracts the characteristic features of the analyzed measurement sequence and creates the feature map. The less visually chaotic the sequence analyzed, the greater the potential for CNN.

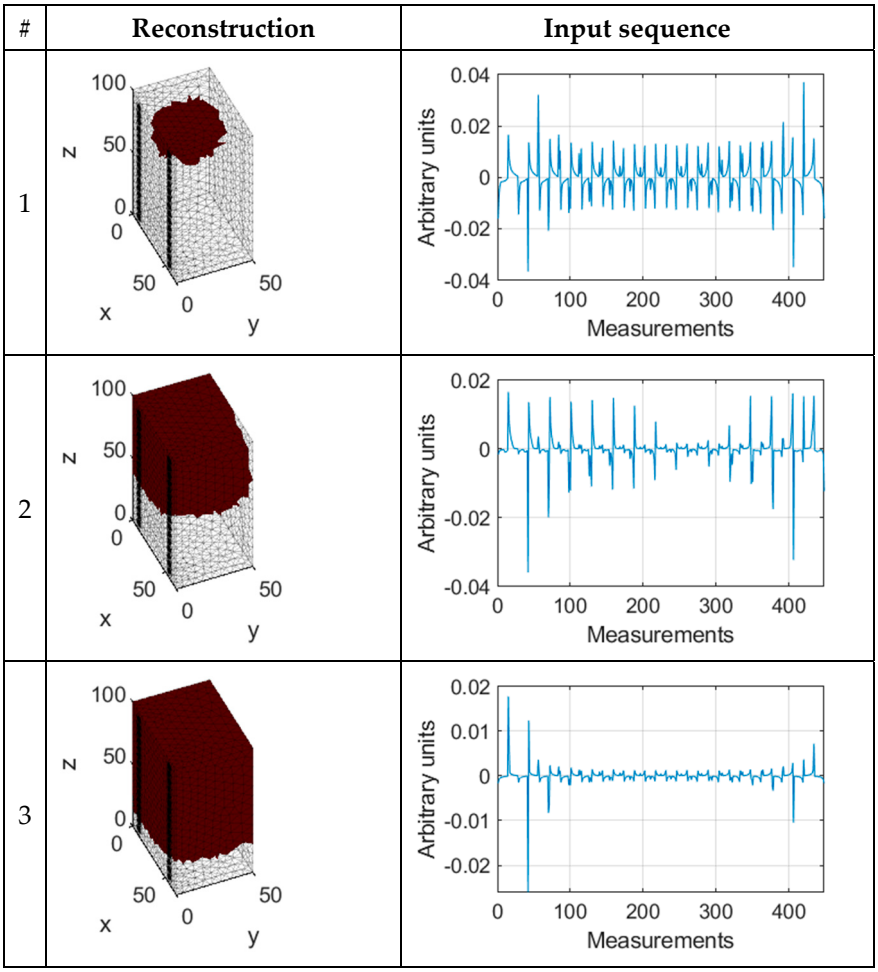


Figure 20. EIT measuring sequences.

Therefore, the analyzed EIT measuring sequences are neither a standard input for CNN (e.g., an image) nor for LSTM (e.g., a non-stationary time sequence). This lack of obviousness creates space for unusual creations, such as the featured CNN+LSTM hybrid model. Experiments with simulation data and reconstructions based on real measurements show that this non-standard approach makes up for the flaws of homogeneous models and creates a synergy effect that improves the quality of the reconstructed images.

4.3. The Concept of Selecting the Optimal Algorithm Using a Model Classifier

Undoubtedly, according to all indicators, the hybrid method CNN+LSTM is the winner. However, as shown in Table 8, it may happen that, in some situations, homogenous methods may turn out to be competitive. For this reason, a classifier was trained, whose task was to select the optimal model (CNN, LSTM or CNN+LSTM) for a given measurement case. It was possible because we already had three trained, ready-to-use models. Figure 21 shows the architecture of the classifier that selects the best image reconstruction model.

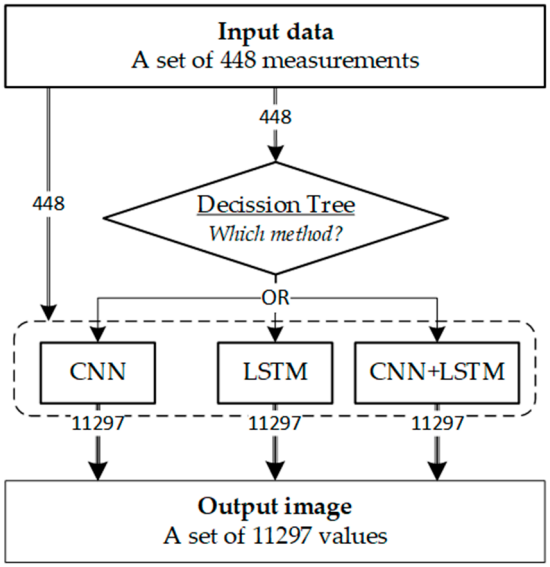


Figure 21. The classifier architecture selects the best model for image reconstruction.

The parameters of the training process were also the same. The hyperparameters of the neural network were changed with the Adam solver based on stochastic optimization [70] with a constant learning rate of 0.001. The classifier used a test set of 10,000 cases as training data. The classifier input has a 448-element measurement vector, similar to the CNN, LSTM and CNN+LSTM models. The output is categorical and consists of three categories that indicate the optimal method (CNN, LSTM or CNN+LSTM). It turned out that this type of classifier achieved an accuracy of 99%. In order to select the best classification method, many variants of classifiers were tested, including *k*-nearest neighbors, decision trees, support vector machines, multilayer perceptron and convolutional neural network classification. Finally, the best accuracy was achieved with the decision tree method. The percentage of correctly classified observations was 99.08%. It is worth noting that the differences in the accuracy of the tested classification methods were not large.

Figure 22 shows the confusion matrix of the model classifier. The classifier correctly indicated 9233 cases of CNN+LSTM, 110 LSTM and 65 CNN wins. The most incorrect classifications (36) concerned cases where the reference category was LSTM, and the model wrongly indicated CNN+LSTM. As a percentage, however, the number of incorrect classifications is negligible.

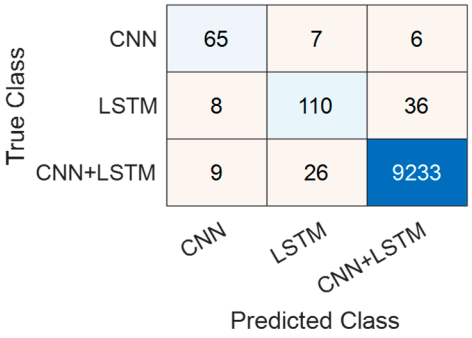


Figure 22. Confusion matrix comparing the methods used.

The above classifier could be used to develop a more complex tomographic system, which, using several prediction methods simultaneously, would optimize the quality of reconstructive images using a specially trained classifier. However, the benefits of using a classifier would be more significant, the less noticeable the dominance of one of the several

available algorithmic methods. Therefore, because CNN+LSTM is so much better, it does not seem necessary to use a classifier if we talk about it.

5. Conclusions

This paper proposes an innovative CNN+LSTM hybrid method for detecting moisture using EIT image reconstruction. Rising energy costs intensify the need to introduce technological solutions to reduce the demand for space heating. Modern technologies in constructing new buildings usually provide thermal insulation and protection against moisture. The problem is the walls of historic buildings, which are not resistant to moisture due to aging processes, a lack of renovation and imperfect construction techniques. With the method shown, it is possible to take the proper steps to lower the energy needed to heat buildings.

The proposed method can take into account the sequence information of the measured set of voltages and enable a more accurate nonlinear representation of voltage and conductivity by combining two popular homogeneous deep learning methods, CNN and LSTM. First, three independent models based on deep neural networks were trained during the research: CNN, LSTM and a hybrid of CNN+LSTM. Then, the methods mentioned above were verified by reconstructing real moisture measurements made in a medieval historical building—the cloisters of the abbey in Pelplin and the reconstruction of cases for which measurements were simulated. Qualitative and quantitative comparisons showed that the hybrid model consisting of both the CNN and LSTM layers is better than the homogeneous CNN and LSTM models.

As mentioned before, tomography is the only method that allows for non-invasive imaging of moisture areas inside the walls of buildings, which justifies the need to improve the EIT. The proposed algorithmic method allows a synergy effect by combining two known methods, CNN and LSTM. The research results showed that the new hybrid CNN+LSTM method made it possible to use the potential of measurement data unavailable for homogeneous methods. Furthermore, the structure of deep neural networks allows the use of different layers and many parallel branches. Therefore, this research shows that using convolutional neural networks and LSTM recurrent networks in parallel is a good way to obtain more accurate EIT reconstructions.

Although the proposed hybrid method achieves good results in EIT image reconstruction, there are still areas that can be improved. The basis of a good reconstruction is an adequately trained model. It cannot be achieved without an adequate amount of good-quality training data. The EIT is a complex process with an uncertain conductivity distribution, so it is helpful to develop training datasets reflecting different test objects. The differences may concern the noise level of the measurement data, the material and structure of the tested wall, differences in moisture levels, etc. Another aspect that can be used to improve the results is implementing multi-branch network architecture, data preprocessing and transfer learning. These are the main directions of our further research on this subject.

Author Contributions: Development of software for mathematical models and the measurement concept of electrical impedance tomography for industrial tomography research, G.K.; Validation, A.H., Development of the system concept, measurement methodology, image reconstruction and supervision, T.R.; Development of a measurement concept in a real model of a tank reactor, preparation of a measuring station, measurements, development of measurement methodology and preparation of descriptions in the article, M.M.; Development of the numerical methods and techniques, K.N.; Literature review, formal analysis, general review and editing of the manuscript, M.R. All authors have read and agreed to the published version of the manuscript.

Funding: This research received no external funding.

Data Availability Statement: Not applicable.

Conflicts of Interest: The authors declare no conflict of interest.

References

1. Stanley, S.J.; Bolton, G.T. A Review of Recent Electrical Resistance Tomography (ERT) Applications for Wet Particulate Processing. *Part. Part. Syst. Charact.* **2008**, *25*, 207–215. [CrossRef]
2. Stacey, R.W.; Li, K.; Horne, R.N. Electrical Impedance Tomography (EIT) Technique for Real-Time Saturation Monitoring. *Proc. SPE Annu. Tech. Conf. Exhib.* **2006**, *6*, 4102–4115. [CrossRef]
3. Zhang, M.; Ma, Y.; Huang, N.; Ge, H. Survey of EIT Image Reconstruction Algorithms. *J. Shanghai Jiaotong Univ. Sci.* **2022**, *27*, 211–218. [CrossRef]
4. Wang, W.; Zhang, P.; Yang, D.; Xue, S. Imaging of Unsaturated Moisture Flow inside Cracked Porous Brick Using Electrical Capacitance Volume Tomography. *J. Build. Eng.* **2023**, *64*, 105626. [CrossRef]
5. Hallaji, M.; Seppänen, A.; Pour-Ghaz, M. Electrical Resistance Tomography to Monitor Unsaturated Moisture Flow in Cementitious Materials. *Cem. Concr. Res.* **2015**, *69*, 10–18. [CrossRef]
6. Smyl, D.; Hallaji, M.; Seppänen, A.; Pour-Ghaz, M. Quantitative Electrical Imaging of Three-Dimensional Moisture Flow in Cement-Based Materials. *Int. J. Heat Mass Transf.* **2016**, *103*, 1348–1358. [CrossRef]
7. Smyl, D.; Hallaji, M.; Seppänen, A.; Pour-Ghaz, M. Three-Dimensional Electrical Impedance Tomography to Monitor Unsaturated Moisture Ingress in Cement-Based Materials. *Transp. Porous Media* **2016**, *115*, 101–124. [CrossRef]
8. Smyl, D.; Rashetnia, R.; Seppänen, A.; Pour-Ghaz, M. Can Electrical Resistance Tomography Be Used for Imaging Unsaturated Moisture Flow in Cement-Based Materials with Discrete Cracks? *Cem. Concr. Res.* **2017**, *91*, 61–72. [CrossRef]
9. Smyl, D. Electrical Tomography for Characterizing Transport Properties in Cement-Based Materials: A Review. *Constr. Build. Mater.* **2020**, *244*, 118299. [CrossRef]
10. Dey, G.; Ganguli, A.; Bhattacharjee, B.; Kumar Gandhi, T. Electrical Response-Based Technique for Estimation of Degree of Moisture Saturation in Cement Concrete and Mortar in Drying and Wetting Cycle. *Constr. Build. Mater.* **2020**, *262*, 120855. [CrossRef]
11. Martínez-Garrido, M.I.; Fort, R.; Gómez-Heras, M.; Valles-Iriso, J.; Varas-Muriel, M.J. A Comprehensive Study for Moisture Control in Cultural Heritage Using Non-Destructive Techniques. *J. Appl. Geophy.* **2018**, *155*, 36–52. [CrossRef]
12. Voss, A.; Hosseini, P.; Pour-Ghaz, M.; Vauhkonen, M.; Seppänen, A. Three-Dimensional Electrical Capacitance Tomography—A Tool for Characterizing Moisture Transport Properties of Cement-Based Materials. *Mater. Des.* **2019**, *181*, 107967. [CrossRef]
13. Yoon, S.; Jeon, D.; Oh, J.-E.; Kim, M.-K.; Kim, D.-J. Experimentally Validated Analytical Solutions to Homogeneous Problems of Electrical Impedance Tomography (EIT) on Rectangular Cement-Based Materials. *Appl. Sci.* **2023**, *13*, 335. [CrossRef]
14. Kłosowski, G.; Maj, M.; Oleszek, M. Comparison of CNN and LSTM Algorithms for Solving the EIT Inverse Problem. *Prz. Elektrotechniczny* **2023**, *99*, 230–233. [CrossRef]
15. Borsoi, R.A.; Aya, J.C.C.; Costa, G.H.; Bermudez, J.C.M. Super-Resolution Reconstruction of Electrical Impedance Tomography Images. *Comput. Electr. Eng.* **2018**, *69*, 1–13. [CrossRef]
16. Hoyle, B.S.; Machin, T.D.; Mohamad-Saleh, J. Machine Learning Process Information from Tomography Data. In *Industrial Tomography: Systems and Applications*, 2nd ed.; Wang, M., Ed.; Woodhead Publishing Series in Electronic and Optical Materials: Leeds, UK, 2022; pp. 427–461. [CrossRef]
17. Wu, X.J.; Xu, M.D.; Li, C.D.; Ju, C.; Zhao, Q.; Liu, S.X. Research on Image Reconstruction Algorithms Based on Autoencoder Neural Network of Restricted Boltzmann Machine (RBM). *Flow Meas. Instrum.* **2021**, *80*, 102009. [CrossRef]
18. da Mata, A.M.M.; de Moura, B.F.; Martins, M.F.; Palma, F.H.S.; Ramos, R. Electrical Conductivity Effect on the Performance Evaluation of EIT Systems: A Review. *Measurement* **2021**, *178*, 109401. [CrossRef]
19. Ren, S.; Sun, K.; Tan, C.; Dong, F. A Two-Stage Deep Learning Method for Robust Shape Reconstruction with Electrical Impedance Tomography. *IEEE Trans. Instrum. Meas.* **2020**, *69*, 4887–4897. [CrossRef]
20. Hrabuska, R.; Prauzek, M.; Venclikova, M.; Konecny, J. Image Reconstruction for Electrical Impedance Tomography: Experimental Comparison of Radial Basis Neural Network and Gauss—Newton Method. *IFAC-PapersOnLine* **2018**, *51*, 438–443. [CrossRef]
21. Fan, Y.; Ying, L. Solving Electrical Impedance Tomography with Deep Learning. *J. Comput. Phys.* **2020**, *404*, 109119. [CrossRef]
22. Gomes, J.C.; Pereira, J.M.S.; de Santana, M.A.; da Silva, W.W.A.; de Souza, R.E.; dos Santos, W.P. Electrical Impedance Tomography Image Reconstruction Based on Autoencoders and Extreme Learning Machines. *Deep. Learn. Data Anal.* **2020**, 155–171. [CrossRef]
23. Bianchessi, A.; Akamine, R.H.; Duran, G.C.; Tanabi, N.; Sato, A.K.; Martins, T.C.; Tsuzuki, M.S.G. Electrical Impedance Tomography Image Reconstruction Based on Neural Networks. *IFAC-PapersOnLine* **2020**, *53*, 15946–15951. [CrossRef]
24. Ghaednia, H.; Owens, C.; Keiderling, L.E.; Hart, J.; Varadarajan, K.; Schwab, J.; Tallman, T.N. Characterization of Interfacial Failure in Cemented Total Joint Replacements via Self-Sensing Bone Cement, Electrical Impedance Tomography, and Machine Learning. *Health Monit. Struct. Biol. Syst. XV* **2021**, *11593*, 252–259. [CrossRef]
25. Fernández-Fuentes, X.; Mera, D.; Gómez, A.; Vidal-Franco, I. Towards a Fast and Accurate EIT Inverse Problem Solver: A Machine Learning Approach. *Electronics* **2018**, *7*, 422. [CrossRef]
26. Aller, M.; Mera, D.; Manuel Cotos, J.; Villaroya, S. Study and Comparison of Different Machine Learning-Based Approaches to Solve the Inverse Problem in Electrical Impedance Tomographies. *Neural Comput. Appl.* **2022**. [CrossRef]
27. Coxson, A.; Mihov, I.; Wang, Z.; Avramov, V.; Barnes, F.B.; Slizovskiy, S.; Mullan, C.; Timokhin, I.; Sanderson, D.; Kretinin, A.; et al. Machine Learning Enhanced Electrical Impedance Tomography for 2D Materials. *Inverse Probl.* **2022**, *38*, 085007. [CrossRef]
28. Aleardi, M.; Vinciguerra, A.; Stucchi, E.; Hojat, A. Probabilistic Inversions of Electrical Resistivity Tomography Data with a Machine Learning-Based Forward Operator. *Geophys. Prospect.* **2022**, *70*, 938–957. [CrossRef]

29. Moghadas, D.; Badorreck, A. Machine Learning to Estimate Soil Moisture from Geophysical Measurements of Electrical Conductivity. *Near Surf. Geophys.* **2019**, *17*, 181–195. [CrossRef]
30. Rymarczyk, T.; Kłosowski, G.; Hoła, A.; Sikora, J.; Wołowiec, T.; Tchórzewski, P.; Skowron, S. Comparison of Machine Learning Methods in Electrical Tomography for Detecting Moisture in Building Walls. *Energies* **2021**, *14*, 2777. [CrossRef]
31. Raimondo, M.; Dondi, M.; Gardini, D.; Guarini, G.; Mazzanti, F. Predicting the Initial Rate of Water Absorption in Clay Bricks. *Constr. Build. Mater.* **2009**, *23*, 2623–2630. [CrossRef]
32. Andreotti, M.; Bottino-Leone, D.; Calzolari, M.; Davoli, P.; Pereira, L.D.; Lucchi, E.; Troi, A. Applied Research of the Hygrothermal Behaviour of an Internally Insulated Historic Wall without Vapour Barrier: In Situ Measurements and Dynamic Simulations. *Energies* **2020**, *13*, 3362. [CrossRef]
33. Lucchi, E.; Pereira, L.D.; Andreotti, M.; Malaguti, R.; Cennamo, D.; Calzolari, M.; Frighi, V. Development of a Compatible, Low Cost and High Accurate Conservation Remote Sensing Technology for the Hygrothermal Assessment of Historic Walls. *Electronics* **2019**, *8*, 643. [CrossRef]
34. Litti, G.; Khoshdel, S.; Audenaert, A.; Braet, J. Hygrothermal Performance Evaluation of Traditional Brick Masonry in Historic Buildings. *Energy Build.* **2015**, *105*, 393–411. [CrossRef]
35. Faysal, R.M.; Bhuiyan, M.M.H.; Al Momin, K.; Tafsirojjaman, T.; Liu, Y. A Review on the Advances of the Study on FRP-Concrete Bond under Hygrothermal Exposure. *Constr. Build. Mater.* **2023**, *363*, 129818. [CrossRef]
36. Hola, A. Measuring of the Moisture Content in Brick Walls of Historical Buildings—The Overview of Methods. *IOP Conf. Ser. Mater. Sci. Eng.* **2017**, *251*, 12067. [CrossRef]
37. Hoła, A.; Matkowski, Z.; Hoła, J. Analysis of the Moisture Content of Masonry Walls in Historical Buildings Using the Basement of a Medieval Town Hall as an Example. *Procedia Eng.* **2017**, *172*, 363–368. [CrossRef]
38. Hoła, A. Methodology for the in Situ Testing of the Moisture Content of Brick Walls: An Example of Application. *Arch. Civ. Mech. Eng.* **2020**, *20*, 3. [CrossRef]
39. Rybak, G.; Strzecha, K.; Krakós, M. A New Digital Platform for Collecting Measurement Data from the Novel Imaging Sensors in Urology. *Sensors* **2022**, *22*, 1539. [CrossRef]
40. Babout, L.; Grudzień, K.; Wiącek, J.; Niedostatkiewicz, M.; Karpiński, B.; Szkodo, M. Selection of Material for X-Ray Tomography Analysis and DEM Simulations: Comparison between Granular Materials of Biological and Non-Biological Origins. *Granul. Matter* **2018**, *20*, 38. [CrossRef]
41. Dusek, J.; Mikulka, J. Measurement-Based Domain Parameter Optimization in Electrical Impedance Tomography Imaging. *Sensors* **2021**, *21*, 2507. [CrossRef]
42. Duraj, A.; Korzeniewska, E.; Krawczyk, A. Classification Algorithms to Identify Changes in Resistance. *Prz. Elektrotechniczny* **2015**, *1*, 82–84. [CrossRef]
43. Szczesny, A.; Korzeniewska, E. Selection of the Method for the Earthing Resistance Measurement. *Prz. Elektrotechniczny* **2018**, *94*, 178–181.
44. Kłosowski, G.; Rymarczyk, T.; Gola, A. Increasing the Reliability of Flood Embankments with Neural Imaging Method. *Appl. Sci.* **2018**, *8*, 1457. [CrossRef]
45. Banasiak, R.; Wajman, R.; Jaworski, T.; Fiderek, P.; Fidos, H.; Nowakowski, J.; Sankowski, D. Study on Two-Phase Flow Regime Visualization and Identification Using 3D Electrical Capacitance Tomography and Fuzzy-Logic Classification. *Int. J. Multiph. Flow* **2014**, *58*, 1–14. [CrossRef]
46. Garbaa, H.; Jackowska-Strumiłło, L.; Grudzień, K.; Romanowski, A. Application of Electrical Capacitance Tomography and Artificial Neural Networks to Rapid Estimation of Cylindrical Shape Parameters of Industrial Flow Structure. *Arch. Electr. Eng.* **2016**, *65*, 657–669. [CrossRef]
47. Kryszyn, J.; Smolik, W. Toolbox for 3D Modelling and Image Reconstruction in Electrical Capacitance Tomography. *Inform. Control. Meas. Econ. Environ. Prot.* **2017**, *7*, 137–145. [CrossRef]
48. Kryszyn, J.; Wanta, D.M.; Smolik, W.T. Gain Adjustment for Signal-to-Noise Ratio Improvement in Electrical Capacitance Tomography System EVT4. *IEEE Sens. J.* **2017**, *17*, 8107–8116. [CrossRef]
49. Majchrowicz, M.; Kapusta, P.; Jackowska-Strumiłło, L.; Sankowski, D. Acceleration of Image Reconstruction Process in the Electrical Capacitance Tomography 3D in Heterogeneous, Multi-GPU System. *Inform. Control. Meas. Econ. Environ. Prot.* **2017**, *7*, 37–41. [CrossRef]
50. Wajman, R.; Fiderek, P.; Fidos, H.; Jaworski, T.; Nowakowski, J.; Sankowski, D.; Banasiak, R. Metrological Evaluation of a 3D Electrical Capacitance Tomography Measurement System for Two-Phase Flow Fraction Determination. *Meas. Sci. Technol.* **2013**, *24*, 065302. [CrossRef]
51. Kłosowski, G.; Hoła, A.; Rymarczyk, T.; Skowron, Ł.; Wołowiec, T.; Kowalski, M. The Concept of Using Lstm to Detect Moisture in Brick Walls by Means of Electrical Impedance Tomography. *Energies* **2021**, *14*, 7617. [CrossRef]
52. Shanghai, J.; Shuang, Y.; Hong, G.; Shenghui, S.; Binbin, L.; Xinyu, H.; Xue, Z.; Mingfu, Z. Study on Reconstruction Algorithm of X-ray Fluorescence Computed Tomography Based on L1/2-Norm and Expectation-Maximum. In Proceedings of the 2021 19th International Conference on Optical Communications and Networks (ICOCN), Qu Fu, China, 23–27 August 2021; pp. 1–3.
53. Kozlowski, E.; Rymarczyk, T.; Klosowski, G. Logistic Regression Application to Image Reconstruction in UST. In Proceedings of the 2019 Applications of Electromagnetics in Modern Engineering and Medicine, PTZE 2019, Janow Podlaski, Poland, 9–12 June 2019.

54. Mikulka, J. GPU-Accelerated Reconstruction of T2 Maps in Magnetic Resonance Imaging. *Meas. Sci. Rev.* **2015**, *15*, 210–218. [CrossRef]
55. Krawczyk, A.; Korzeniewska, E. Magnetophosphenes—History and Contemporary Implications. *Prz. Elektrotechniczny* **2018**, *1*, 63–66. [CrossRef]
56. Soleimani, M.; Adler, A.; Dai, T.; Peyton, A.J. Application of a Single Step Temporal Imaging of Magnetic Induction Tomography for Metal Flow Visualisation. *Insight Non-Destr. Test. Cond. Monit.* **2008**, *50*, 25–29. [CrossRef]
57. Korzeniewska, E.; Sekulska-Nalewajko, J.; Gocławski, J.; Dróżdż, T.; Kiełbasa, P. Analysis of Changes in Fruit Tissue after the Pulsed Electric Field Treatment Using Optical Coherence Tomography. *Eur. Phys. J. Appl. Phys.* **2020**, *91*, 30902. [CrossRef]
58. Rząsa, M.R. Selection of Optical Tomography Parameters for Gas Bubble Shape Analysis. *Chem. Process Eng. Inz. Chem. Proces.* **2014**, *35*, 19–33. [CrossRef]
59. Rymarczyk, T.; Kłosowski, G.; Hoła, A.; Hoła, J.; Sikora, J.; Tchórzewski, P.; Skowron, Ł. Historical Buildings Dampness Analysis Using Electrical Tomography and Machine Learning Algorithms. *Energies* **2021**, *14*, 1307. [CrossRef]
60. Liu, S.; Jia, J.; Zhang, Y.D.; Yang, Y. Image Reconstruction in Electrical Impedance Tomography Based on Structure-Aware Sparse Bayesian Learning. *IEEE Trans. Med. Imaging* **2018**, *37*, 2090–2102. [CrossRef]
61. Kabanikhin, S.I. Definitions and Examples of Inverse and Ill-Posed Problems. *J. Inverse Ill Posed Probl.* **2008**, *16*, 317–357. [CrossRef]
62. Adler, A.; Lionheart, W.R.B. Uses and Abuses of EIDORS: An Extensible Software Base for EIT. *Physiol. Meas.* **2006**, *27*, S25–S42. [CrossRef]
63. Liu, D.; Zhao, Y.; Khambampati, A.K.; Seppänen, A.; Du, J. A Parametric Level Set Method for Imaging Multiphase Conductivity Using Electrical Impedance Tomography. *IEEE Trans. Comput. Imaging* **2018**, *4*, 552. [CrossRef]
64. Rymarczyk, T.; Kłosowski, G.; Kozłowski, E. A Non-Destructive System Based on Electrical Tomography and Machine Learning to Analyze the Moisture of Buildings. *Sensors* **2018**, *18*, 2285. [CrossRef] [PubMed]
65. Rymarczyk, T.; Kozłowski, E.; Tchórzewski, P.; Kłosowski, G.; Adamkiewicz, P. Applying the Logistic Regression in Electrical Impedance Tomography to Analyze Conductivity of the Examined Objects. *Int. J. Appl. Electromagn. Mech.* **2020**, *64*, S235–S252. [CrossRef]
66. Liu, S.; Wu, H.; Huang, Y.; Yang, Y.; Jia, J. Accelerated Structure-Aware Sparse Bayesian Learning for Three-Dimensional Electrical Impedance Tomography. *IEEE Trans. Industr. Inform.* **2019**, *15*, 5033–5041. [CrossRef]
67. Tang, H.; Xu, C.; Han, X. Electrical Resistance Tomography Image Reconstruction Based on One-Dimensional Multi-Branch Convolutional Neural Network Combined with Attention Mechanism. *Flow Meas. Instrum.* **2022**, *84*, 102140. [CrossRef]
68. Jasiulewicz-Kaczmarek, M.; Antosz, K.; Wyczółkowski, R.; Mazurkiewicz, D.; Sun, B.; Qian, C.; Ren, Y. Application of MICMAC, Fuzzy AHP, and Fuzzy TOPSIS for Evaluation of the Maintenance Factors Affecting Sustainable Manufacturing. *Energies* **2021**, *14*, 1436. [CrossRef]
69. Rymarczyk, T.; Kłosowski, G.; Hoła, A.; Sikora, J.; Tchórzewski, P.; Skowron, Ł. Optimising the Use of Machine Learning Algorithms in Electrical Tomography of Building Walls: Pixel Oriented Ensemble Approach. *Measurement* **2022**, *188*, 110581. [CrossRef]
70. Kingma, D.P.; Ba, J.L. Adam: A Method for Stochastic Optimization. In Proceedings of the 3rd International Conference on Learning Representations, ICLR 2015—Conference Track Proceedings, San Diego, CA, USA, 7–9 May 2015.

Disclaimer/Publisher's Note: The statements, opinions and data contained in all publications are solely those of the individual author(s) and contributor(s) and not of MDPI and/or the editor(s). MDPI and/or the editor(s) disclaim responsibility for any injury to people or property resulting from any ideas, methods, instructions or products referred to in the content.